Riemann problem for the light pulses in optical fibers for the generalized Chen-Lee-Liu equation

Sergey K. Ivanov

Moscow Institute of Physics and Technology, Institutsky Lane 9, Dolgoprudny, Moscow Region 141700, Russia and Institute of Spectroscopy, Russian Academy of Sciences, Troitsk, Moscow 108840, Russia

(Received 11 January 2020; accepted 16 April 2020; published 12 May 2020)

We provide the classification of possible wave structures evolving from initially discontinuous profiles for the photon fluid propagating in a normal dispersion fiber. The dynamics of light fields is described by the generalized Chen-Lee-Liu equation, which belongs to the family of the nonlinear Schrödinger equations with a self-steepening-type term appearing due to retardation of the fiber material response to variations of the electromagnetic signal. This equation is also used in investigations of the dynamics of modulated waves propagating through a single nonlinear transmission network. We describe its periodic solutions and the corresponding Whitham modulation equations. The wave patterns generated by the initial parameter profiles are composed of different building blocks which are presented in detail. It is shown that evolution dynamics in this case is much richer than that for the nonlinear Schrödinger equation. Complete classification of possible wave structures is given for all possible jump conditions at the discontinuity. Our analytic results are confirmed by numerical simulations.

DOI: 10.1103/PhysRevA.101.053827

I. INTRODUCTION

The evolution of light pulses in waveguides is a subject of active modern experimental and theoretical research. One of the trends in this field is the study of so-called dispersive shock waves. Such structures are observed in various physical media, such as water waves (where such waves are often called undular bores), Bose-Einstein condensates, waves in magnetics and in nonlinear optics, and other areas of physics (see, e.g., [1,2]). It is well known that if one neglects the effects of dissipation and dispersion, then the theory of nonlinear propagation of light envelopes suffers from a wave-breaking singularity developed at some finite fiber length after which a formal solution of nonlinear wave equations becomes multivalued and loses its physical meaning. The account of dispersion eliminates such a nonphysical behavior. But the evolution equations for the envelopes acquire higher-order derivatives, and after the wave-breaking moment, instead of the multivalued region, an expanding region of fast nonlinear oscillations is formed. Envelope parameters in such a structure change slowly compared with the characteristic oscillation frequency and their wavelength. This region of fast oscillations is called the "dispersive shock wave" (DSW).

One of the most substantial problems in which DSWs can occur is the *Riemann problem*, which includes classification of wave structures resulting from the evolution of the initial discontinuity. This problem has played an important role since the classical paper of Riemann [3], subsequently supplemented by the jump conditions of Rankin [4] and Hugoniot [5,6]; it served as a prototype of the example of shock formation in dispersionless media with small viscosity. The full classification of possible wave patterns evolving from initial discontinuities was obtained by Kotchine [7]. However, in the case of optical systems, we have dispersion instead of viscosity. The problem where DSWs are formed instead of viscous shocks was studied for the first time in the context of the physics of shallow water waves whose evolution is described by the celebrated Korteweg–de Vries (KdV) equation [8]. The equations governing the slow evolution of the envelope of the nonlinear oscillations had been derived by Whitham [9] and they were applied to the description of the DSW structure by Gurevich and Pitaevskii [10]. Because of the universality of the KdV equation, this approach can naturally be applied to many other physical situations. Later it became clear [11] that the diagonalization of the Whitham modulation equations is possible due to the special property discovered in [12] of the complete integrability of the KdV equation. Development of the finite-gap integration method [13,14], as well as the methods of deriving [11,15] and solving the Whitham equations [16,17], made it possible to extend the Gurevich-Pitaevskii approach to a number of other completely *integrable* equations of physical interest (see, for instance, [2]) and it admits investigation of *non-genuinely-nonlinear* hyperbolic systems.

In nonlinear optics, DSWs were observed long ago (see, e.g., [18,19]), but they remain the subject of active current experimental (see, e.g., [20–22]) and theoretical (see, e.g., [23,24]) research. In the fiber optics applications, the dynamics of pulses is usually described by the nonlinear Schrödinger (NLS) equation that accounts for two main effects: quadratic normal dispersion and Kerr nonlinearity. For this case, the theory of DSWs is already well developed and the main parameters of the arising wave structures can be calculated for typical idealized situations in simple analytical form. Extension of the Gurevich-Pitaevskii approach to the NLS equation became possible only after derivation of the Whitham modulation equations [25,26] by the methods based on the inverse scattering transform for the NLS equation [27], which means its complete integrability. In particular, consideration of many realistic problems can be reduced to analysis of the so-called

Riemann problem of evolution of discontinuity in the initial data. Such a discontinuity can appear, for example, as a jump in the time dependence of the light intensity, which is mostly typical in physics of light pulses in fibers, or evolve from a "collision" of two pulses in which case not only intensity has a discontinuity but also the time and space derivatives of the phase. Classification of possible wave structures in the NLS equation theory was given in Refs. [28,29], and it provides the theoretical basis for calculation of characteristic parameters of such experiments as that of Ref. [30]. It was shown that the NLS theory evolution of any initial discontinuity leads to a wave pattern consisting of a sequence of building blocks, two of which are represented by either the rarefaction wave or the DSW. However, in nonlinear optics, besides quadratic dispersion and Kerr nonlinearity, many other effects can play important role in the propagation of pulses. For instance, in experiment [31] with photorefractive material the saturation of nonlinearity is quite essential and the corresponding theory of DSWs was developed in Ref. [32]. Naturally, in order to get a better understanding of the higher-order nonlinear effects, it is necessary to introduce several other higher-order terms, such as third-order dispersion, quintic nonlinear terms, etc., into the Hirota equation [33], Kundu-Eckhaus equation [34,35], Lakshmanan-Porsezian-Daniel equation [36], and a generalized NLS equation [37]. Due to recent technological developments in laser and ultrahigh-bit-rate optical fiber communication, these higher-order nonlinear effects are unavoidable in many optical systems when modeling the transmission of ultrashort and high-intensity light pulses in nonlinear optical media. In fiber optics, one needs to take into account such effects as dissipation, higher-order dispersion, intrapulse Raman scattering, and self-steepening (see, e.g., [38]). These effects can drastically change evolution of DSWs, leading sometimes to violation of the supposition that such an evolution is adiabatically slow. Theoretically, the self-steepening term that arises in optical settings is commonly associated with the class of the derivative nonlinear Schrödinger (DNLS) equation. It is relevant to mention that the self-steepening of an optical fiber pulse, otherwise called Kerr dispersion, arises when the group velocity of a pulse depends on the intensity [39]. Several versions of the DNLS equations have been studied from different points of view. Well known NLS equations with derivative terms include the Kaup-Newell equation [40], the Chen-Lee-Liu equation [41], and the Gerjikov-Ivanov equation [42], which arise in theories of nonlinear optics, fluid dynamics, and plasma physics. These nonlinear wave equations are usually called DNLS-I, DNLS-II, and DNLS-III equations, respectively. The pulse propagation in a single-mode optical fiber can be described by the Chen-Lee-Liu (CLL) equation

$$iq_t + \tfrac{1}{2}q_{xx} + i\delta|q|^2 q_x = 0, \tag{1}$$

where the coordinates t and x denote propagation distance and retarded time, but represent slow time and spatial coordinate traveling with group velocity in hydrodynamics, respectively. In optical fiber setting, the term involving parameter $\delta > 0$ is usually associated with the self-steepening phenomena [43]. In Ref. [44] Moses *et al.* performed optical pulse propagation involving self-steepening without self-phase-modulation. This experiment provides the first experimental evidence of the CLL equation. The CLL equation (1) corresponds to a situation where the dispersionless Riemann invariants depend nonmonotonically on the physical variables; that is, the problem is not genuinely nonlinear (see, e.g., [45]). In this case, new types of wave structures arise, which are similar to contact discontinuities in the theory of viscous shock waves. So the CLL equation can be considered as an example of *nonconvex dispersive hydrodynamics*.

We consider the propagation of an optical pulse inside a monomode fiber modeled by a *generalized Chen-Lee-Liu* (generalized CLL) equation,

$$iq_t + \tfrac{1}{2}q_{xx} - |q|^2 q + i\delta|q|^2 q_x = 0, \tag{2}$$

that also includes the Kerr nonlinearity, which is inevitable at sufficiently high intensities. The generalized CLL equation is simply related to the CLL equation (see, e.g., [46]). This equation is also used in the investigation of modulated wave dynamics of waves propagating through a single nonlinear transmission network, which also presents practical interest (see [47] and references therein).

Motivated by applications of the generalized CLL equation (2), we consider the method which permits one to predict a wave pattern arising from any given data for an initial discontinuity. The method is quite general and it was applied to the generalized NLS equations with self-steepening nonlinearity [48,49] and to the Landau-Lifshitz equation for magnetics with easy-plane anisotropy (or polarization waves in a two-component Bose-Einstein condensate) [50]. Here we extend the theory to the non-genuine-case of the generalized CLL equation (2). The exact integrability of this equation makes it possible to develop a Whitham modulational theory for describing configurations where nonlinear waves are slowly modulated, as observed in dispersive shocks.

The paper is organized as follows: The influence of the last term of the generalized CLL equation (2) on the dynamics of linear waves that propagate along a uniform background and small-amplitude limit is discussed in Sec. II. The exact integrability of this equation is used in Sec. III for derivation of the Whitham modulational equations. In Sec. IV we describe the elementary wave structures that appear as building blocks in the general wave patterns. The full classification of the solutions of the Riemann problem is presented in Sec. V. The Sec. VI is devoted to conclusions.

II. LINEAR WAVES AND SMALL-DISPERSION AND WEAK-NONLINEARITY LIMITS

Let us turn to the study of linear waves and the small-amplitude and weak-dispersion limits when these two effects are taken into account in the main approximation. That is, we are interested in propagation of disturbances along a uniform background intensity ρ_0. To this end, it is convenient to use the physical variables of intensity $\rho(x,t)$ and chirp $u(x,t)$. To go to the equations for these variables, we apply the Madelung transform

$$q(x,t) = \sqrt{\rho(x,t)}\exp\left[i\int^x u(x',t)dx'\right]. \tag{3}$$

After its substitution into Eq. (2), separation of the real and imaginary parts, and differentiation of one of the equations

with respect to x, we get the system

$$\rho_t + \left(\rho u + \frac{1}{2}\delta\rho^2\right)_x = 0,$$
$$u_t + uu_x + \rho_x + \delta(\rho u)_x + \left(\frac{\rho_x^2}{8\rho^2} - \frac{\rho_{xx}}{4\rho}\right)_x = 0. \quad (4)$$

The last term on the left-hand side of the second equation describes the dispersion.

The linear dispersion relation of the system (4) for linear waves propagating along a constant background ρ_0 has the form

$$\omega_{1,2}(k) = \left(\delta\rho_0 \pm \sqrt{\frac{k^2}{4} + \rho_0}\right)k. \quad (5)$$

Here ω is the frequency of the linear waves and k is the wave number. Suppose that at the initial moment the phase of the wave is constant and there is only the intensity perturbation. After standard calculations we get the solution of the linear problem expressed in terms of the Fourier transform $\widehat{\rho_0}'(k)$ of the initial (input) intensity linear disturbance,

$$\rho'(x,t) = \frac{1}{4\pi}\int_{-\infty}^{+\infty} \widehat{\rho_0}'(k)[e^{i(kx-\omega_1 t)} + e^{i(kx-\omega_2 t)}]dk. \quad (6)$$

One can see that an initial pulse splits into two smaller pulses; however, in contrast to the NLS case, two pulses propagate with different group velocities. This is a manifestation of lack of the x-inversion invariance, which is caused by the last term in the generalized CLL equation (2).

We are interested in the leading dispersion and nonlinear corrections to the dispersionless linear propagation of disturbances. Using the system (4) and applying the standard perturbation theory for the amplitude of the perturbation and for the weak dispersion (see, for example, [1]), one can obtain a small-amplitude analog of Eq. (2). Let the wave propagate in the positive direction of the x axis. Then an approximate equation for $\rho' = \rho - \rho_0$ takes the form

$$\frac{\partial\rho'}{\partial t} + (\delta\rho_0 + \sqrt{\rho_0})\frac{\partial\rho'}{\partial x} + \frac{3}{2}\frac{1+\delta\sqrt{\rho_0}}{\delta\sqrt{\rho_0}}\delta\rho'\frac{\partial\rho'}{\partial x} - \frac{1}{8\sqrt{\rho_0}}\frac{\partial^3\rho'}{\partial x^3} = 0. \quad (7)$$

This is the Korteweg–de Vries (KdV) equation. Formation of DSWs from initial discontinuities in the KdV equation theory has been well known since the pioneering paper Ref. [10]: the initial discontinuity evolves into either a rarefaction wave or a cnoidal DSW. In the limit $\delta\sqrt{\rho} \to 1$ the nonlinear term of Eq. (7) has finite value and we need not include higher-order corrections for taking into account higher-order nonlinear effects. The situation is the opposite for another simple wave propagating in the negative direction of the x axis. In this case we have the Gardner equation

$$\frac{\partial\rho'}{\partial t} + (\delta\rho_0 - \sqrt{\rho_0})\frac{\partial\rho'}{\partial x} - \frac{3}{2}\frac{1-\delta\sqrt{\rho_0}}{\delta\sqrt{\rho_0}}\delta\rho'\frac{\partial\rho'}{\partial x} + \frac{3}{8}\frac{1+\delta\sqrt{\rho_0}}{\rho_0^{3/2}}\rho'^2\frac{\partial\rho'}{\partial x} + \frac{1}{8\sqrt{\rho_0}}\frac{\partial^3\rho'}{\partial x^3} = 0. \quad (8)$$

In the limit $\delta\sqrt{\rho} \to 1$ the last equation reduces to the modified Korteweg–de Vries (mKdV) equation

$$\frac{\partial\rho'}{\partial t} + \frac{3}{4\rho_0^{3/2}}\rho'^2\frac{\partial\rho'}{\partial x} + \frac{1}{8\sqrt{\rho_0}}\frac{\partial^3\rho'}{\partial x^3} = 0. \quad (9)$$

The situation for the mKdV and Gardner equations is much more complicated than for the KdV case [51] and in this case we can get eight different structures including, besides the rarefaction waves and cnoidal DSWs, also trigonometric DSWs, combined shocks and their combinations separated by plateaus. Therefore one should expect that in the case of the Riemann problem for Eq. (2) we also have to get much richer structure than in the NLS case. To solve this problem, at first we have to find periodic solutions of Eq. (2) in a form that is convenient for us, that is, in a form parametrized by the parameters related to the Riemann invariants of the corresponding Whitham modulation equations by simple formulas. In the next section we shall obtain the periodic solutions by this method and derive the Whitham equations.

III. PERIODIC SOLUTIONS AND WHITHAM MODULATION EQUATIONS

The finite-gap integration method (see, e.g., [1]) is based on the possibility of representing the generalized CLL equation (2) as a compatibility condition of two systems of linear equations with a spectral parameter λ,

$$\frac{\partial}{\partial x}\begin{pmatrix}\psi_1\\ \psi_2\end{pmatrix} = \begin{pmatrix}F & G\\ H & -F\end{pmatrix}\begin{pmatrix}\psi_1\\ \psi_2\end{pmatrix}, \quad (10)$$
$$\frac{\partial}{\partial t}\begin{pmatrix}\psi_1\\ \psi_2\end{pmatrix} = \begin{pmatrix}A & B\\ C & -A\end{pmatrix}\begin{pmatrix}\psi_1\\ \psi_2\end{pmatrix}, \quad (11)$$

where

$$F = -\frac{i}{2\delta}(\lambda^2 - \delta^2|q|^2 + 1), \quad G = -q\lambda, \quad H = q^*\lambda,$$
$$A = -\frac{i}{4\delta^2}(\lambda^2 - \delta^2|q|^2 + 1)^2 - \frac{\delta}{4}(q_x q^* - q q_x^*) - \frac{i}{2}|q|^2,$$
$$B = -\frac{1}{2\delta}(\lambda^2 - \delta^2|q|^2 + 1)q\lambda - \frac{i}{2}q_x\lambda,$$
$$C = \frac{1}{2\delta}(\lambda^2 - \delta^2|q|^2 + 1)q^*\lambda - \frac{i}{2}q_x^*\lambda. \quad (12)$$

This Lax pair can be obtained by simple transformation from the known Lax pair for the CLL equation (1) (see Ref. [52]). The 2×2 linear problems (10) and (11) have two linearly independent basis solutions which we denote as $(\psi_1, \psi_2)^T$ and $(\varphi_1, \varphi_2)^T$. We define the "squared basis functions"

$$f = -\frac{i}{2}(\psi_1\varphi_2 + \psi_2\varphi_1), \quad g = \psi_1\varphi_1, \quad h = -\psi_2\varphi_2, \quad (13)$$

which obey the linear equations

$$f_x = iGh - iHg, \quad (14a)$$
$$g_x = 2Fg + 2iGf, \quad (14b)$$
$$h_x = -2Fh - 2iHf, \quad (14c)$$

and

$$f_t = iBh - iCg, \tag{15a}$$
$$g_t = 2Ag + 2iBf, \tag{15b}$$
$$h_t = -2Ah - 2iCf. \tag{15c}$$

We look for the solutions of these equations in the form

$$\begin{aligned} f &= (\lambda^2 - \delta^2|q|^2 + 1)^2 - f_1(\lambda^2 - \delta^2|q|^2 + 1) + f_2, \\ g &= -2\delta(\lambda^2 - \delta^2|q|^2 + 1 - \mu)q\lambda, \\ h &= 2\delta(\lambda^2 - \delta^2|q|^2 + 1 - \mu^*)q^*\lambda. \end{aligned} \tag{16}$$

Here the functions $f_1(x,t)$, $f_2(x,t)$, $\mu(x,t)$, and $\mu^*(x,t)$ are unknown; $\mu(x,t)$ and $\mu^*(x,t)$ are not interrelated *a priori*, but we shall find soon that they are complex conjugate, whence the notation.

Substitution of Eqs. (16) into Eqs. (14) gives after equating the coefficients of like powers of λ expressions for the x derivatives of f_1 and f_2,

$$f_{1,x} = 0, \qquad f_{2,x} = \delta^2(2 - 2\delta^2|q|^2 - f_1)(|q|^2)_x, \tag{17}$$

and of $|q|^2$ and μ,

$$\begin{aligned} (|q|^2)_x &= \frac{i}{\delta}(\mu - \mu^*)|q|^2, \\ (\mu q)_x &= -i\delta(\mu - \mu^*)|q|^2 - \frac{i}{\delta}f_2 q. \end{aligned} \tag{18}$$

In a similar way, substitution of (16) into (15) with account of (17) gives equations for the t derivatives of f_1 and f_2,

$$f_{1,t} = 0, \quad f_{2,t} = \frac{f_1}{2\delta}f_{2,x}, \tag{19}$$

and

$$(|q|^2)_t = \frac{f_1}{2\delta}(|q|^2)_x. \tag{20}$$

It is easy to check that the expression $f^2 - gh = P(\lambda)$ does not depend on x and t; however it can depend on the spectral parameter λ. We are interested in the one-phase periodic solution. It is distinguished by the condition that $P(\lambda)$ is an eighth-degree polynomial of the form

$$\begin{aligned} f^2 - gh = P(\lambda) &= \prod_{i=1}^{4}\left(\lambda^2 - \lambda_i^2\right) \\ &= \lambda^8 - s_1\lambda^6 + s_2\lambda^4 - s_3\lambda^2 + s_4. \end{aligned} \tag{21}$$

Equating the coefficients of like powers of λ at two sides of this identity, we get

$$s_1 = 2f_1 - 4, \tag{22a}$$
$$\begin{aligned} s_2 = {} & f_1^2 + 2f_2 - 4\delta^2|q|^2(\mu + \mu^*) \\ & + 2[3f_1 - 3 - \delta^2|q|^2][\delta^2|q|^2 - 1], \end{aligned} \tag{22b}$$
$$\begin{aligned} s_3 = {} & \left(s_2 + f_1^2 + 2f_2 + 2[\delta^4|q|^4 - 1]\right)[\delta^2|q|^2 - 1] \\ & + 2f_1f_2 - 4\delta^2|q|^2\mu\mu^*, \end{aligned} \tag{22c}$$
$$s_4 = ([f_1 + \delta^2|q|^2 - 1][\delta^2|q|^2 - 1] + f_2)^2. \tag{22d}$$

Here s_i are standard symmetric functions of the four zeros λ_i^2 of the polynomial $P(\lambda)$:

$$\begin{aligned} & s_1 = \sum_i \lambda_i^2, \quad s_2 = \sum_{i<j}\lambda_i^2\lambda_j^2, \quad s_3 = \sum_{i<j<k}\lambda_i^2\lambda_j^2\lambda_k^2, \\ & s_4 = \lambda_1^2\lambda_2^2\lambda_3^2\lambda_4^2. \end{aligned} \tag{23}$$

Equations (22) allow us to express μ, μ^* as functions of $|q|^2$. The first and the last Eqs. (22) give

$$\begin{aligned} f_1 &= \frac{s_1}{2} + 2, \\ f_2 &= 1 - \delta^4|q|^4 - \frac{s_1}{2}(\delta^2|q|^2 - 1) \pm \sqrt{s_4}. \end{aligned} \tag{24}$$

We substitute that into (22b) and (22c) and obtain the system for μ and μ^*, which can be easily solved to give

$$\begin{aligned} \mu = \frac{1}{2\delta^2|q|^2}\Bigg[& \left(\frac{s_1}{4}\right)^2 + \frac{1}{2}\delta^2|q|^2(s_1 + 4 - 2\delta^2|q|^2) \\ & - \frac{s_2}{4} \pm \frac{1}{2}\sqrt{s_4} - i\sqrt{-\mathcal{R}(\delta^2|q|^2)}\Bigg], \end{aligned} \tag{25}$$

where

$$\begin{aligned} \mathcal{R}(\nu) = {} & \nu^4 + s_1\nu^3 + \left(\frac{3}{8}s_1^2 - \frac{s_2}{2} \mp 3\sqrt{s_4}\right)\nu^2 \\ & + \left(\frac{1}{16}s_1^3 + s_3 - \frac{1}{4}s_1s_2 \mp \frac{1}{2}s_1\sqrt{s_4}\right)\nu \\ & + \left[\left(\frac{s_1}{4}\right)^2 - \frac{s_2}{4} \pm \frac{1}{2}\sqrt{s_4}\right]^2. \end{aligned} \tag{26}$$

The function $\mathcal{R}$ introduced here is a fourth-degree polynomial in ν and it is called an *algebraic resolvent* of the polynomial $P(\lambda)$, because zeros of $\mathcal{R}(\nu)$ are related to zeros of $P(\lambda)$ by the following simple symmetric expressions: the upper sign in (26) corresponds to the zeros

$$\begin{aligned} \nu_1 &= \tfrac{1}{4}(-\lambda_1 + \lambda_2 + \lambda_3 - \lambda_4)^2, \\ \nu_2 &= \tfrac{1}{4}(\lambda_1 - \lambda_2 + \lambda_3 - \lambda_4)^2, \\ \nu_3 &= \tfrac{1}{4}(\lambda_1 + \lambda_2 - \lambda_3 - \lambda_4)^2, \\ \nu_4 &= \tfrac{1}{4}(\lambda_1 + \lambda_2 + \lambda_3 + \lambda_4)^2, \end{aligned} \tag{27}$$

and the lower sign in Eq. (26) corresponds to the zeros

$$\begin{aligned} \nu_1 &= \tfrac{1}{4}(-\lambda_1 + \lambda_2 + \lambda_3 + \lambda_4)^2, \\ \nu_2 &= \tfrac{1}{4}(\lambda_1 - \lambda_2 + \lambda_3 + \lambda_4)^2, \\ \nu_3 &= \tfrac{1}{4}(\lambda_1 + \lambda_2 - \lambda_3 + \lambda_4)^2, \\ \nu_4 &= \tfrac{1}{4}(\lambda_1 + \lambda_2 + \lambda_3 - \lambda_4)^2. \end{aligned} \tag{28}$$

This can be proved by a simple check of the Vieta formulas.

As follows from the second Eq. (19), the first Eq. (24) gives the expression for the constant phase velocity,

$$\begin{aligned} V &= -\frac{f_1}{2\delta} = -\frac{1}{\delta} - \frac{s_1}{4\delta} \\ &= -\frac{1}{\delta} - \frac{1}{4\delta}\sum_{i=1}^{4}\lambda_i^2 = -\frac{1}{\delta} - \frac{1}{4\delta}\sum_{i=1}^{4}\nu_i, \end{aligned} \tag{29}$$

and we find that f_2 depends on $\xi = x - Vt$ only. Then from Eq. (20) we see that the intensity $\rho = |q|^2$ also depends only on ξ. The equations for dynamics of ρ can be easily found by substitution of (25) into the first Eq. (18), so we get

$$\frac{d(\delta^2\rho)}{d\xi} = \frac{1}{\delta}\sqrt{-\mathcal{R}(\delta^2\rho)}, \tag{30}$$

where $\mathcal{R}$ is, as we know, a fourth-degree polynomial with the zeros given in terms of λ_i by the formulas (27) or (28). This equation can be solved in a standard way in terms of elliptic functions. Without going to much detail we shall present here the main results.

We shall assume that λ_i are ordered according to $0 \leqslant \lambda_1 \leqslant \lambda_2 \leqslant \lambda_3 \leqslant \lambda_4$ and then both our definitions (27) and (28) give the same ordering of ν_i: $\nu_1 \leqslant \nu_2 \leqslant \nu_3 \leqslant \nu_4$. The real solutions correspond to oscillations of $\delta^2\rho$ within the intervals where $-\mathcal{R}(\delta^2\rho) \geqslant 0$.

(A) At first we shall consider the periodic solution corresponding to oscillations of $\delta^2\rho$ in the interval

$$\nu_1 \leqslant \delta^2\rho \leqslant \nu_2. \tag{31}$$

Standard calculation yields, after some algebra, the solution in terms of Jacobi elliptic functions:

$$\delta^2\rho = \nu_2 - \frac{(\nu_2-\nu_1)\mathrm{cn}^2(\theta,m)}{1+\frac{\nu_2-\nu_1}{\nu_4-\nu_2}\mathrm{sn}^2(\theta,m)}, \tag{32}$$

where it is assumed that $\delta^2\rho(0) = \nu_1$,

$$\theta = \sqrt{(\nu_3-\nu_1)(\nu_4-\nu_2)}\,\xi/(2\delta), \tag{33}$$

$$m = \frac{(\nu_4-\nu_3)(\nu_2-\nu_1)}{(\nu_4-\nu_2)(\nu_3-\nu_1)}, \tag{34}$$

the functions cn and sn being Jacobi elliptic functions [53]. The period of oscillations along the x axis is equal to function (32) and is

$$L = \frac{4K(m)}{\sqrt{(\nu_3-\nu_1)(\nu_4-\nu_2)}} = \frac{4K(m)}{\sqrt{(\lambda_3^2-\lambda_1^2)(\lambda_4^2-\lambda_2^2)}}, \tag{35}$$

where $K(m)$ is the complete elliptic integral of the first kind [53].

In the limit $\nu_3 \to \nu_2$ ($m \to 1$) the period tends to infinity and the solution (32) acquires the soliton form

$$\delta^2\rho = \nu_2 - \frac{\nu_2-\nu_1}{\cosh^2\theta + \frac{\nu_2-\nu_1}{\nu_4-\nu_2}\sinh^2\theta}. \tag{36}$$

This is a "dark soliton" for the variable ρ.

The limit $m \to 0$ can be reached in two ways.

(i) If $\nu_2 \to \nu_1$, then the solution transforms into a linear harmonic wave,

$$\begin{aligned}\delta^2\rho &\cong \nu_2 - \tfrac{1}{2}(\nu_2-\nu_1)\cos(\omega\xi/\delta),\\ \omega &= \sqrt{(\nu_3-\nu_1)(\nu_4-\nu_1)}.\end{aligned} \tag{37}$$

(ii) If $\nu_4 = \nu_3$ but $\nu_1 \neq \nu_2$, then we arrive at the nonlinear trigonometric solution:

$$\begin{aligned}\delta^2\rho &= \nu_2 - \frac{(\nu_2-\nu_1)\cos^2\theta}{1+\frac{\nu_2-\nu_1}{\nu_3-\nu_2}\sin^2\theta},\\ \theta &= \sqrt{(\nu_3-\nu_1)(\nu_3-\nu_2)}\,\xi/(2\delta).\end{aligned} \tag{38}$$

If we take the limit $\nu_2 - \nu_1 \ll \nu_3 - \nu_1$ in this solution, then we return to the small-amplitude limit (37) with $\nu_4 = \nu_3$. On the other hand, if we take here the limit $\nu_2 \to \nu_3 = \nu_4$, then the argument of the trigonometric functions becomes small and we can approximate them by the first terms of their series expansions. This corresponds to an algebraic soliton of the form

$$\delta^2\rho = \nu_2 - \frac{\nu_2-\nu_1}{1+(\nu_2-\nu_1)^2\xi^2/(4\delta^2)}. \tag{39}$$

(B) In the second case, the variable $\delta^2\rho$ oscillates in the interval

$$\nu_3 \leqslant \delta^2\rho \leqslant \nu_4. \tag{40}$$

Here again, a standard calculation yields

$$\delta^2\rho = \nu_3 + \frac{(\nu_4-\nu_3)\mathrm{cn}^2(\theta,m)}{1+\frac{\nu_4-\nu_3}{\nu_3-\nu_1}\mathrm{sn}^2(\theta,m)} \tag{41}$$

with the same definitions (33), (34), and (35) for θ, m, and T, correspondingly. In this case we have $\delta^2\rho(0) = \nu_4$. In the soliton limit $\nu_3 \to \nu_2$ ($m \to 1$) we get

$$\delta^2\rho = \nu_2 + \frac{\nu_4-\nu_2}{\cosh^2\theta + \frac{\nu_4-\nu_2}{\nu_2-\nu_1}\sinh^2\theta}. \tag{42}$$

This is a "bright soliton" for the variable ρ.

Again, the limit $m \to 0$ can be reached in two ways.

(i) If $\nu_4 \to \nu_3$, then we obtain a small-amplitude harmonic wave

$$\begin{aligned}\delta^2\rho &\cong \nu_3 + \tfrac{1}{2}(\nu_4-\nu_3)\cos(\omega\xi/\delta),\\ \omega &= \sqrt{(\nu_3-\nu_1)(\nu_3-\nu_2)}.\end{aligned} \tag{43}$$

(ii) If $\nu_2 = \nu_1$, then we obtain another nonlinear trigonometric solution,

$$\begin{aligned}\delta^2\rho &= \nu_3 + \frac{(\nu_4-\nu_3)\cos^2\theta}{1+\frac{\nu_4-\nu_3}{\nu_3-\nu_1}\sin^2\theta},\\ \theta &= \sqrt{(\nu_3-\nu_1)(\nu_4-\nu_1)}\,\xi/(2\delta).\end{aligned} \tag{44}$$

If we assume that $\nu_4 - \nu_3 \ll \nu_4 - \nu_1$, then this reproduces the small-amplitude limit (43) with $\nu_2 = \nu_1$. On the other hand, in the limit $\nu_3 \to \nu_2 = \nu_1$ we obtain the algebraic soliton solution:

$$\delta^2\rho = \nu_1 + \frac{\nu_4-\nu_1}{1+(\nu_4-\nu_1)^2\xi^2/(4\delta^2)}. \tag{45}$$

The convenience of this form of periodic solutions of our equation is related to the fact that the parameters λ_i, connected with ν_i by the formulas (27), (28), play the role of Riemann invariants in the Whitham theory of modulations. For both cases (27), (28) we have the identities

$$m = \frac{(\nu_4-\nu_3)(\nu_2-\nu_1)}{(\nu_4-\nu_2)(\nu_3-\nu_1)} = \frac{(\lambda_4^2-\lambda_3^2)(\lambda_2^2-\lambda_1^2)}{(\lambda_4^2-\lambda_2^2)(\lambda_3^2-\lambda_1^2)}. \tag{46}$$

Now we shall consider slowly modulated waves. In this case, the parameters λ_i ($i = 1, 2, 3, 4$) become slowly varying functions of x and t changing little in one period and they can serve as Riemann invariants. Evolution of λ_i is governed by

the Whitham modulation equations

$$\frac{\partial\lambda_i}{\partial t}+v_i\frac{\partial\lambda_i}{\partial x}=0,\quad i=1,2,3,4. \tag{47}$$

The Whitham velocities appearing in these equations can be computed by means of the formula

$$v_i=\left(1-\frac{L}{\partial_i L}\partial_i\right)V,\quad \text{where}\quad \partial_i\equiv\frac{\partial}{\partial\lambda_i^2}, \tag{48}$$

with the use of Eqs. (29) and (35). Hence, a simple calculation yields the explicit expressions

$$\begin{aligned}
v_1&=-\frac{1}{\delta}+\frac{1}{4\delta}\sum_{i=1}^{4}\lambda_i^2-\frac{1}{2\delta}\frac{(\lambda_4^2-\lambda_1^2)(\lambda_2^2-\lambda_1^2)K(m)}{(\lambda_4^2-\lambda_1^2)K(m)-(\lambda_4^2-\lambda_2^2)E(m)},\\
v_2&=-\frac{1}{\delta}+\frac{1}{4\delta}\sum_{i=1}^{4}\lambda_i^2+\frac{1}{2\delta}\frac{(\lambda_3^2-\lambda_2^2)(\lambda_2^2-\lambda_1^2)K(m)}{(\lambda_3^2-\lambda_2^2)K(m)-(\lambda_3^2-\lambda_1^2)E(m)},\\
v_3&=-\frac{1}{\delta}+\frac{1}{4\delta}\sum_{i=1}^{4}\lambda_i^2-\frac{1}{2\delta}\frac{(\lambda_4^2-\lambda_3^2)(\lambda_3^2-\lambda_2^2)K(m)}{(\lambda_3^2-\lambda_2^2)K(m)-(\lambda_4^2-\lambda_2^2)E(m)},\\
v_4&=-\frac{1}{\delta}+\frac{1}{4\delta}\sum_{i=1}^{4}\lambda_i^2+\frac{1}{2\delta}\frac{(\lambda_4^2-\lambda_3^2)(\lambda_4^2-\lambda_1^2)K(m)}{(\lambda_4^2-\lambda_1^2)K(m)-(\lambda_3^2-\lambda_1^2)E(m)},
\end{aligned} \tag{49}$$

where $E(m)$ is the complete elliptic integral of the second kind [53].

In a modulated wave representing a dispersive shock wave, the Riemann invariants change with x and t. The dispersive shock wave occupies a space interval at which edges two of the Riemann invariants coincide. The soliton edge corresponds to $\lambda_3=\lambda_2$ $(m=1)$ and at this edge the Whitham velocities are given by

$$\begin{aligned}
v_1&=-\frac{1}{\delta}+\frac{1}{4\delta}(3\lambda_1^2+\lambda_4^2),\\
v_2=v_3&=-\frac{1}{\delta}+\frac{1}{4\delta}(\lambda_1^2+2\lambda_2^2+\lambda_4^2),\\
v_4&=-\frac{1}{\delta}+\frac{1}{4\delta}(\lambda_1^2+3\lambda_4^2).
\end{aligned} \tag{50}$$

The small-amplitude limit $m=0$ can be obtained in two ways. If $\lambda_3=\lambda_4$, then we get

$$\begin{aligned}
&v_1=-\frac{1}{\delta}+\frac{1}{4\delta}(3\lambda_1^2+\lambda_2^2),\quad v_2=-\frac{1}{\delta}+\frac{1}{4\delta}(\lambda_1^2+3\lambda_2^2),\\
&v_3=v_4=-\frac{1}{\delta}+\frac{1}{\delta}\lambda_4^2+\frac{1}{4\delta}\frac{(\lambda_2^2-\lambda_1^2)^2}{\lambda_1^2+\lambda_2^2-2\lambda_4^2},
\end{aligned} \tag{51}$$

and if $\lambda_2=\lambda_1$, then

$$\begin{aligned}
&v_1=v_2=-\frac{1}{\delta}+\frac{1}{\delta}\lambda_1^2-\frac{1}{4\delta}\frac{(\lambda_4^2-\lambda_3^2)^2}{\lambda_3^2+\lambda_4^2-2\lambda_1^2},\\
&v_3=-\frac{1}{\delta}+\frac{1}{4\delta}(3\lambda_3^2+\lambda_4^2),\quad v_4=-\frac{1}{\delta}+\frac{1}{4\delta}(\lambda_3^2+3\lambda_4^2).
\end{aligned} \tag{52}$$

We can now proceed to the description of key elements ("building blocks") from which the wave patterns are constructed.

IV. KEY ELEMENTS

We consider in the present paper the so-called Riemann problem. This corresponds to the study of the evolution of initial discontinuous profiles of the form

$$\begin{aligned}
\rho(t=0)&=\begin{cases}\rho^L, & x<0,\\ \rho^R, & x>0,\end{cases}\\
u(t=0)&=\begin{cases}u^L, & x<0,\\ u^R, & x>0.\end{cases}
\end{aligned} \tag{53}$$

Evolution of such a pulse leads to formation of quite complex structures consisting of simpler elements. We shall describe these elements in the present section.

A. Rarefaction waves

For smooth enough wave patterns we can neglect the last dispersion term in the second equation of the system (4) and arrive at the so-called dispersionless equations

$$\begin{aligned}
&\rho_t+\left(\rho u+\tfrac{1}{2}\delta\rho^2\right)_x=0,\\
&u_t+uu_x+\rho_x+\delta(\rho u)_x=0.
\end{aligned} \tag{54}$$

First of all, this system admits a trivial solution for which $\rho=$ constant and $u=$ constant. We shall call such a solution a "plateau." It is convenient to transform the system (54) to a diagonal Riemann form,

$$\frac{\partial r_\pm}{\partial t}+v_\pm\frac{\partial r_\pm}{\partial x}=0, \tag{55}$$

by defining the Riemann invariants and Riemann velocities

$$\begin{aligned}
r_\pm&=\frac{u}{2}+\frac{\delta\rho}{2}\pm\sqrt{(1+\delta u)\rho},\\
v_\pm&=u+\delta\rho\pm\sqrt{(1+\delta u)\rho},
\end{aligned} \tag{56}$$

where the Riemann velocities are expressed via the Riemann invariants by the relations

$$v_+=\tfrac{3}{2}r_++\tfrac{1}{2}r_-,\quad v_-=\tfrac{1}{2}r_++\tfrac{3}{2}r_-. \tag{57}$$

It is clear that the system is modulationally unstable if

$$u<-\frac{1}{\delta}. \tag{58}$$

A rarefaction wave belongs to the class of simple wave solutions. For such a solution, one of the Riemann invariants is constant, and this condition either $r_+=$ constant or $r_-=$ constant gives, when applied to Eqs. (56), the relationship between the variables ρ and u. Consequently, on the (u,ρ) plane these simple wave solutions are depicted as curves (see Fig. 1)

$$\rho=\frac{2+2\delta r_\pm+\delta u\pm2\sqrt{(1+2\delta r_\pm)(1+\delta u)}}{\delta^2}. \tag{59}$$

To have the intensity positive, it is necessary to fulfill the condition $-1/(2\delta)\leqslant r_-\leqslant r_+$. Both curves touch the boundary line $u=-1/\delta$ of the instability region. In Fig. 1, the modulationally unstable region (58) is gray. Along the line $\rho=(1+\delta u)/\delta^2$ both derivatives $\partial r_+/\partial u=0$, $\partial r_+/\partial\rho=0$ vanish. We say that this line separates two monotonicity regions in the half plane $\rho\geqslant0$ (see Fig. 1). The two intersection

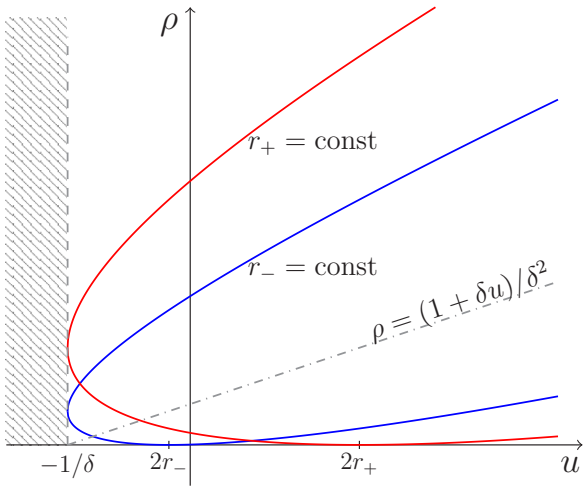

FIG. 1. Relation between ρ and u for the simple wave solutions in the dispersionless regime. One line corresponds to $r_- =$ constant (blue), and another one to $r_+ =$ constant (red). Gray area shows the modulationally unstable region $u < -1/\delta$.

points of curves correspond to uniform flows with constant parameters $\rho =$ constant and $u =$ constant, that is, to the plateau solutions. It is easy to express the physical variables ρ and u in terms of r_- and r_+,

$$\rho(\zeta) = \frac{1}{2\delta^2}[1 + \delta(r_+ + r_-) \pm \sqrt{(1+2\delta r_+)(1+2\delta r_-)}],$$
$$u = \frac{1}{2\delta}[\delta(r_+ + r_-) - 1 \mp \sqrt{(1+2\delta r_+)(1+2\delta r_-)}]. \quad (60)$$

The initial profiles (53), being infinitely sharp, do not involve any characteristic length. Therefore the large-scale features of the solution of this problem can depend on the self-similar variable $\zeta = x/t$ only, that is, $r_\pm = r_\pm(\zeta)$, and then the system (55) reduces to

$$(v_- - \zeta)\frac{dr_-}{d\zeta} = 0, \quad (v_+ - \zeta)\frac{dr_+}{d\zeta} = 0. \quad (61)$$

We note again that these equations have a simple solution $r_- =$ constant, $r_+ =$ constant with constant u and ρ, which corresponds to the above-mentioned plateau region.

Turning to self-similar simple wave solutions, let us consider for definiteness the case when $r_- =$ constant. Then r_+ changes in such a way that the term between parentheses in the right equation (61) is zero ($v_+ = \zeta$), so we have

$$\rho = \frac{1}{2\delta^2}\left\{1 + \frac{2}{3}\delta r_- + \frac{2}{3}\delta\zeta \pm \sqrt{(1+2\delta r_-)\left(1 - \frac{2}{3}\delta r_- + \frac{4}{3}\delta\zeta\right)}\right\},$$
$$u(\zeta) = \frac{2}{3}(r_- + \zeta) - \delta\rho(\zeta). \quad (62)$$

We see that in the self-similar solutions the variable ζ must be above its minimal value,

$$\zeta \geqslant \frac{r_-}{2} - \frac{3}{4\delta}. \quad (63)$$

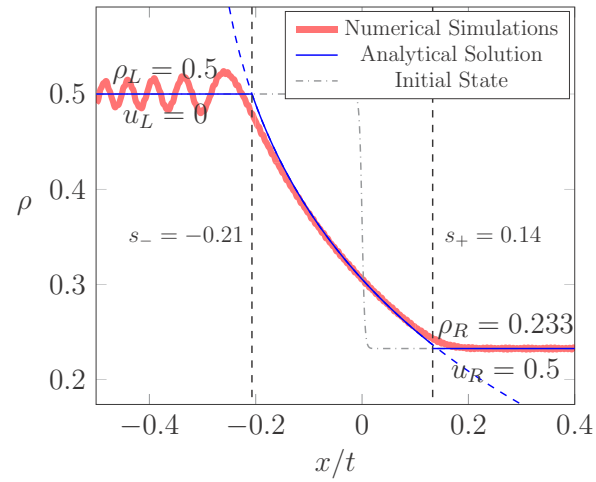

FIG. 2. Dependence of simple wave solution $\rho(\zeta)$ on $\zeta = x/t$ composed by a rarefaction wave connecting two uniform flows. Numerical solution is shown in red (thick) and analytical solution is shown in blue (thin). Vertical dashed lines indicate the edges of the rarefaction wave according to (66). Gray dash-dotted line represents the initial state. Here $\rho^L = 0.5$, $u^L = 5$, $\rho^R = 0.233$, $u^R = 0.5$, with $\delta = 1$.

Similar formulas and plots can be obtained for the solution $r_+ =$ constant, $v_-(r_-, r_+) = x/t \equiv \zeta$. This wave configuration represents a rarefaction wave. In the general case this type of wave can connect uniform flows with equal values of the corresponding Riemann invariants $r_-^L = r_-^R$ or $r_+^L = r_+^R$. An example of the corresponding distribution is shown in Fig. 2. The analytical simple wave approximation (thin blue) agrees with the numerical solution of the generalized CLL equation (2) (thick red) very well.

It is clear that in these self-similar solutions one of the Riemann invariants must be constant and another one must increase with ζ according to

$$r_- = r_-^0 = \text{const}, \quad v_+ = \tfrac{3}{2}r_+ + \tfrac{1}{2}r_-^0 = \zeta, \quad (64)$$

or

$$r_+ = r_+^0 = \text{const}, \quad v_- = \tfrac{3}{2}r_- + \tfrac{1}{2}r_+^0 = \zeta. \quad (65)$$

The dependence of the Riemann invariants on the physical parameters must also be monotonic in order to keep the solution single-valued. The dependence of the Riemann invariants on ζ is sketched in Fig. 3 for two possible situations with r_- or r_+ constant. The edge velocities of these rarefaction waves are equal to

$$\text{(a)} \quad s_- = \tfrac{1}{2}r_-^L + \tfrac{3}{2}r_+^L, \quad s_+ = \tfrac{1}{2}r_-^R + \tfrac{3}{2}r_+^R;$$
$$\text{(b)} \quad s_- = \tfrac{3}{2}r_-^L + \tfrac{1}{2}r_+^L, \quad s_+ = \tfrac{3}{2}r_-^R + \tfrac{1}{2}r_+^R. \quad (66)$$

Obviously, the corresponding wave structures must satisfy the conditions (a) $r_+^L < r_+^R$, $r_-^L = r_-^R$ or (b) $r_+^L = r_+^R$, $r_-^L < r_-^R$. The other two situations with opposite inequalities result in multivalued solutions and are therefore nonphysical: the dispersionless approximation is not applicable to these cases and we have to turn to another type of key element for describing such structures.

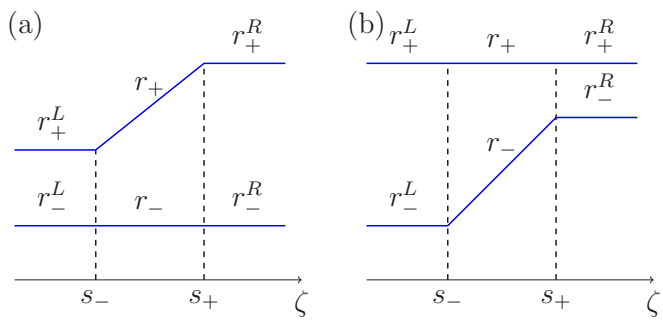

FIG. 3. Diagrams representing the evolution of the Riemann invariants as a function of $\zeta = x/t$ for two types of rarefaction waves.

B. Cnoidal dispersive shock waves

The other two possible solutions of Eqs. (55) are sketched in Fig. 4, where for future convenience we have made the change $r \mapsto \lambda$ ($r_\pm$ will be functions of $\lambda_\pm$ defined below), and they satisfy the boundary conditions (a) $\lambda_+^L = \lambda_+^R$, $\lambda_-^L > \lambda_-^R$ or (b) $\lambda_+^L > \lambda_+^R$, $\lambda_-^L = \lambda_-^R$. We consider λ_i as four Riemann invariants of the Whitham system that describe evolution of a modulated nonlinear periodic wave. We interpret this as a formation of the cnoidal dispersive shock wave from the initial discontinuity with such a type of the boundary conditions.

Since the pioneering work of Gurevich and Pitaevskii [10], it has been known that wave breaking is regularized by the replacement of the nonphysical multivalued dispersionless solution by a dispersive shock wave. This wave pattern can be represented approximately as a modulated nonlinear periodic wave in which parameters λ_i change slowly along the wave structure. In this case, the two dispersionless Riemann invariants $\lambda_\pm$ (or $r_\pm$) are replaced in the DSW region by four Riemann invariants λ_i. In this region, the evolution of the DSW is determined by the Whitham equations (47). If we consider a self-similar solution, then all Riemann invariants depend only on $\zeta = x/t$, and the Whitham equations reduce to

$$(v_i - \zeta)\frac{d\lambda_i}{d\zeta} = 0, \quad i = 1, 2, 3, 4. \tag{67}$$

Hence we find again that only one Riemann invariant varies along the DSW, while the other three are constant;

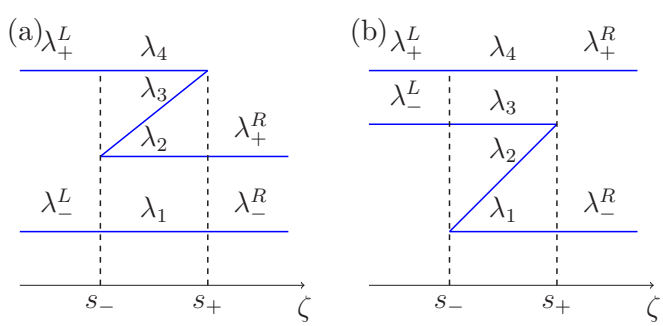

FIG. 4. Diagrams considered within the dispersionless approximation correspond to a formal multivalued solution. In this case, the dispersionless approximation breaks down and one observes a dispersive shock wave, accurately described by four Riemann invariants within the Whitham modulational approach.

that is, the corresponding diagram reproduces the picture shown in Fig. 4. The limiting expressions (50) for the Whitham velocities must coincide with expressions (57) for dispersionless Riemann velocities and therefore we can relate the corresponding dispersionless and dispersive Riemann invariants by the formulas

$$\begin{aligned} &\text{(a)} \quad \lambda_-^L = \sqrt{1+2\delta r_-}, \quad \lambda_+^L = \sqrt{1+2\delta r_+}, \\ &\text{(b)} \quad \lambda_-^R = \sqrt{1+2\delta r_-}, \quad \lambda_+^R = \sqrt{1+2\delta r_+}, \end{aligned} \tag{68}$$

at the soliton edges of the DSW. Here $r_\pm^{L,R}$ are the Riemann invariants of the dispersionless theory that are defined by Eqs. (56). They describe the plateau solution at the soliton edge of the DSW. In a similar way, at the small-amplitude edges we find similar relations

$$\text{(a)} \quad \lambda_-^R = \sqrt{1+2\delta r_-}, \quad \lambda_+^R = \sqrt{1+2\delta r_+}, \tag{69}$$

and

$$\text{(b)} \quad \lambda_-^L = \sqrt{1+2\delta r_-}, \quad \lambda_+^L = \sqrt{1+2\delta r_+}. \tag{70}$$

Again the limiting expressions (51) and (52) coincide with the dispersionless expressions (57). Then the self-similar solutions of the Whitham equations (67) are given by

$$\begin{aligned} &\text{(a)} \quad v_3(\lambda_-^L, \lambda_+^R, \lambda_3(\zeta), \lambda_+^L) = \zeta, \\ &\text{or} \\ &\text{(b)} \quad v_2(\lambda_-^R, \lambda_2(\zeta), \lambda_-^L, \lambda_+^L) = \zeta, \end{aligned} \tag{71}$$

which define the dependence of the Riemann invariants (modulation parameters) λ_3 or λ_2 on ζ in implicit form. The edges of the DSW propagate with velocities

$$\begin{aligned} \text{(a)} \quad s_- &= -\frac{1}{\delta} + \frac{1}{4\delta}[(\lambda_-^L)^2 + 2(\lambda_+^R)^2 + (\lambda_+^L)^2], \\ s_+ &= -\frac{1}{\delta} + \frac{1}{\delta}(\lambda_+^L)^2 + \frac{1}{4\delta}\frac{[(\lambda_+^R)^2 - (\lambda_-^R)^2]^2}{(\lambda_+^R)^2 + (\lambda_-^R)^2 - 2(\lambda_+^L)^2}, \\ \text{(b)} \quad s_- &= -\frac{1}{\delta} + \frac{1}{\delta}(\lambda_+^R)^2 + \frac{1}{4\delta}\frac{[(\lambda_+^L)^2 - (\lambda_-^L)^2]^2}{(\lambda_+^L)^2 + (\lambda_-^L)^2 - 2(\lambda_+^R)^2}, \\ s_+ &= -\frac{1}{\delta} + \frac{1}{4\delta}[(\lambda_-^R)^2 + 2(\lambda_+^L)^2 + (\lambda_+^R)^2]. \end{aligned} \tag{72}$$

As shown in the diagrams of Fig. 4, three of the four Riemann invariants λ_i in the DSW are equal to the values of Riemann invariants on the boundaries. Moreover, the third invariant changes according to (71). The substitution of λ_i determines the dependence of v_i on ζ for each of the cases in (27) and (28). This means that there are two mappings from Riemann invariants to the physical parameters. This point will be important in classification of the wave structures evolved from the initial discontinuities. For example, let us consider the case (a) ($\lambda_-^L = \lambda_-^R$, $\lambda_+^L > \lambda_+^R$). We have two paths on the (u, I) plane that satisfy this choice. These two paths $L_1 \to R_1$ and $L_2 \to R_2$ are shown in Fig. 5 and correspond to two mappings (27) and (28), where points L_1 and L_2 correspond to the left boundary condition with the Riemann invariants equal to λ_-^L and λ_+^L, and the points R_1 and R_2 correspond to the right boundary condition with the Riemann invariants equal to λ_-^R and λ_+^R. In Fig. 6 we compare the analytic solution in the

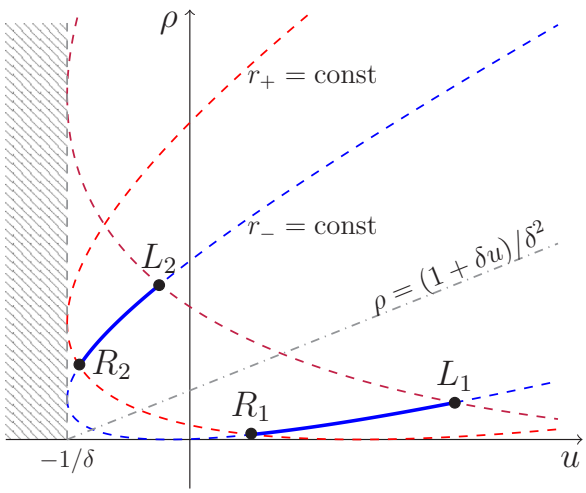

FIG. 5. Example of two possible paths in the (u, ρ) plane between the left and right boundary for the case of dispersive shock waves. Corresponding wave structures are shown in Fig. 6 and they satisfy the same solution of the Whitham equations, but different boundary conditions in physical variables.

Whitham approximation with the exact numerical solution of the generalized CLL equation. One can see that the envelope functions resulting from the Whitham approach (dashed black lines) agree very well with the exact numerical solution (thick red lines).

In a similar way, the diagram Fig. 4(b) produces two other wave structures.

C. Contact dispersive shock waves

We now turn to the study of the situation where the left and right boundary points belong to different monotonicity regions. First, we consider the situation in which the Riemann invariants have equal values at both edges of the shock, i.e., when $r_-^L = r_-^R$, $r_+^L = r_+^R$ and, consequently, $\lambda_-^L = \lambda_-^R$, $\lambda_+^L = \lambda_+^R$. This situation resembles the one of the so called "contact discontinuities" which play an important role in the theory of viscous shocks (see, e.g., Ref. [54]); therefore we shall denote the wave structures arising in this case as *contact dispersive shock waves* (to avoid any confusion, we should mention that in the dynamics of immiscible condensates, interfaces between two components may appear which play the same role as the one played by contact discontinuities in the theory of viscous shocks; see, e.g., [55]). This type of DSW was first reported in [56] where the evolution of a step problem was studied for the focusing mKdV equation (see also a similar solution for the complex modified mKdV equation in [57]). In [58] these (trigonometric) DSWs were first attributed the name of contact DSWs. The contact DSWs of the generalized CLL equation are described by the modulated finite-amplitude nonlinear periodic solutions (38) or (44). At one of the edges of the trigonometric shock the amplitude vanishes and at the opposite edge it assumes some finite value. Generically, as will be explained later, contact DSWs are realized as parts of composite solutions (either a combination of cnoidal and trigonometric shocks or a combination of a trigonometric

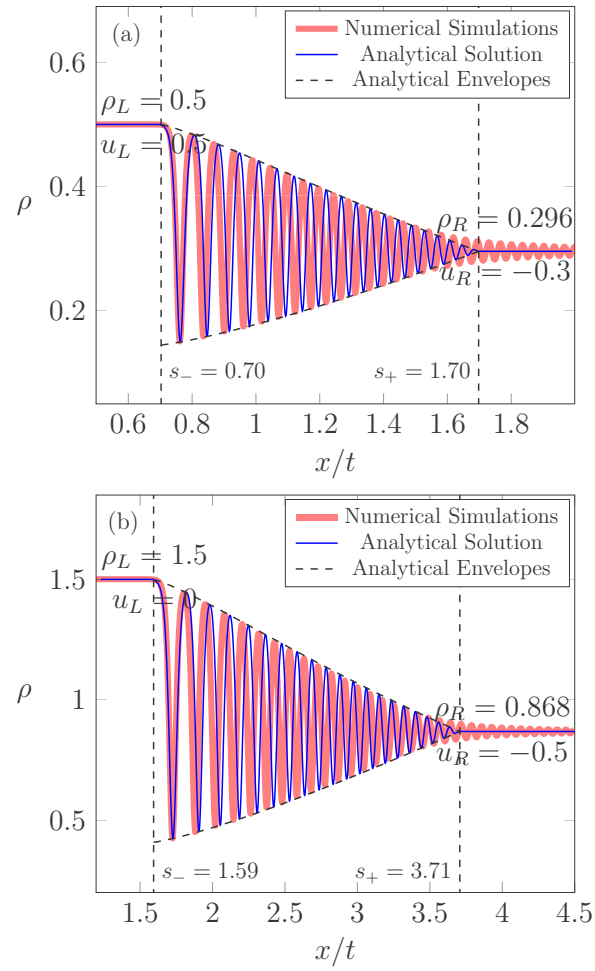

FIG. 6. The comparison of analytical (thin blue) and numerical (thick red) solutions of the generalized CLL equation (2) for two different boundary conditions and the same solution of the Whitham equations for the modulation parameters: (a) $\rho^L = 0.5$, $u^L = 0.5$, $\rho^R = 0.296$, $u^R = -0.3$; (b) $\rho^L = 1.5$, $u^L = 0$, $\rho^R = 0.868$, $u^R = -0.5$ with $\delta = 1$. Dashed lines show analytical envelopes. Vertical dashed lines indicate the edges of the cnoidal DSW wave according to (72).

DSW and a rarefaction wave). Such contact waves can arise only if the boundary points are located on the opposite sides of the line $\rho = (1 + \delta u)/\delta^2$, i.e., in different regions of monotonicity. The diagram shown in Fig. 7 corresponds to the path in Fig. 8. In this case, the curve connecting the end points crosses the line $\rho = (1 + \delta u)/\delta^2$ of the hyperbolicity square along which λ_- takes its minimal value: $\lambda_- = 0$. This means that in the formal dispersionless solution, the invariant λ_- would first decrease and reach its minimal value, then increase to the initial value along the same "path." We see in Fig. 7 that two Riemann invariants λ_3 and λ_4 are constant within the shock region and they match the boundary condition $\lambda_3 = \lambda_-^L = \lambda_-^R$, $\lambda_4 = \lambda_+^L = \lambda_+^R$, whereas the two other Riemann invariants are equal to each other ($\lambda_1 = \lambda_2$) and satisfy the same Whitham equation with $v_1(\lambda_1, \lambda_1, \lambda_-^L, \lambda_+^L) = v_2(\lambda_1, \lambda_1, \lambda_-^L, \lambda_+^L) = \zeta$. Here ζ varies within the interval $s_- \leqslant$

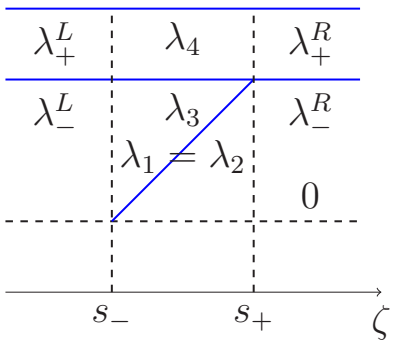

FIG. 7. Diagram represents evolution of the Riemann invariants as functions of $\zeta = x/t$ in the contact DSW solution of the Whitham equations: $r_-^L = r_-^R$ ($\lambda_-^L = \lambda_-^R$), $r_+^L = r_+^R$ ($\lambda_+^L = \lambda_+^R$).

$\zeta \leqslant s_+$ with

$$s_- = -\frac{1}{\delta} - \frac{1}{4\delta}\frac{[(\lambda_+^L)^2 - (\lambda_-^L)^2]^2}{(\lambda_-^L)^2 + (\lambda_+^L)^2},$$
$$s_+ = -\frac{1}{\delta} + \frac{1}{4\delta}[3(\lambda_-^R)^2 + (\lambda_+^R)^2]. \tag{73}$$

As in the case of cnoidal DSWs, due to different mappings (27) or (28) the single contact diagram corresponds to two DSW structures. An example of two paths $P_1 \to P_2$ and the opposite $P_2 \leftarrow P_1$ is shown in Fig. 8. The corresponding wave structures are shown in Fig. 9. For the contact DSW the wave amplitude varies in a quadratic manner through the shock. This is particularly noticeable near the small-amplitude edge of the DSW. This is in contrast to the cnoidal DSW for which the wave amplitude varies linearly.

D. Combined shocks

It is natural to ask what happens if one of the Riemann invariants still remains constant ($r_+^L = r_+^R$ or $\lambda_+^L = \lambda_+^R$); however the boundary values of the other Riemann invariant are

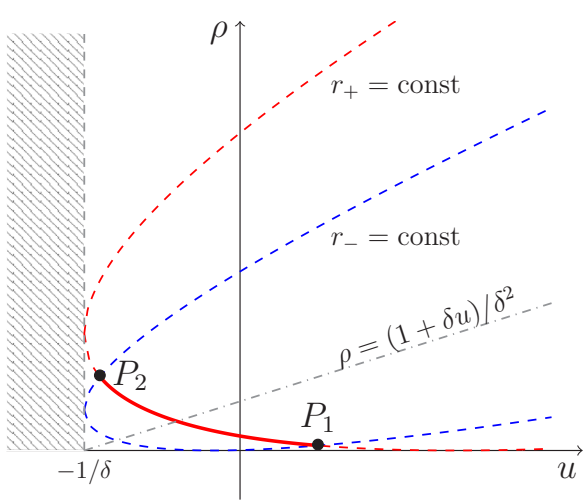

FIG. 8. Example of path for a contact DSW ($r_+^L = r_+^R$ and $r_-^L = r_-^R$) with crossing of $\rho = (1 + \delta u)/\delta^2$ line separating the regions of monotonicity. Two directions $P_1 \leftrightarrow P_2$ are described by the mappings (27) and (28).

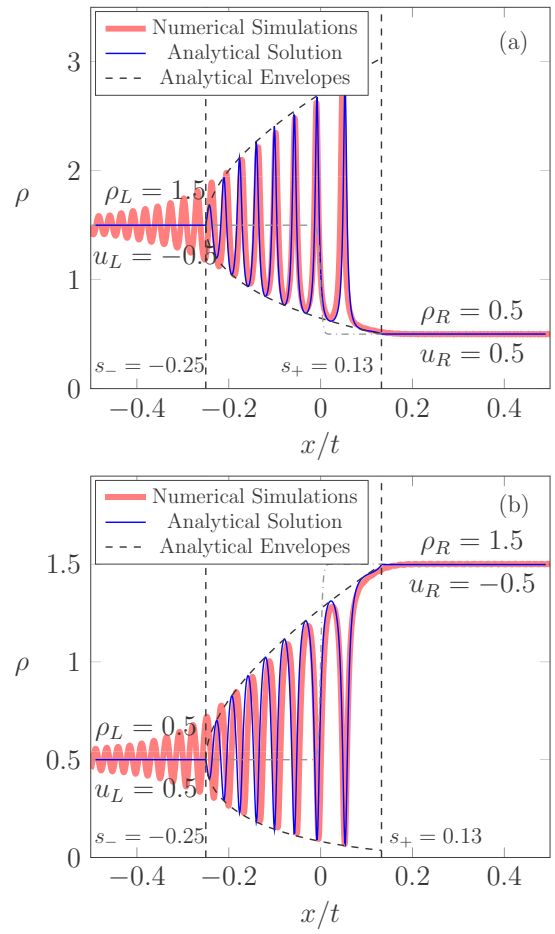

FIG. 9. The comparison of analytical (thin blue) and numerical (thick red) solutions of the generalized CLL equation (2) for contact DSW for two possible choices of directions $P_1 \longleftrightarrow P_2$ and corresponding mappings (27) and (28). Here (a) $\rho^L = 1.5$, $u^L = -0.5$, $\rho^R = 0.5$, $u^R = 0.5$; (b) $\rho^L = 0.5$, $u^L = 0.5$, $\rho^R = 1.5$, $u^R = -0.5$ with $\delta = 1$. Dashed black lines show analytical envelopes; gray dash-dotted line represents the initial state. Vertical dashed lines indicate the edges of the contact DSW wave according to (73).

different: $r_-^L < r_-^R$ ($\lambda_-^L > \lambda_-^R$) or $r_-^L > r_-^R$ ($\lambda_-^L < \lambda_-^R$). To be definite, we shall consider two generalizations of the situation. The transition of the type $L_1 \to R_1$ or $L_2 \to R_2$ of Fig. 8 can be generalized in two ways represented in Fig. 10, where the points L_i and R_i symbolize plateaus at the left and right boundaries, respectively. In this case the boundary points are also located in different monotonicity regions. Diagrams for Riemann invariants for both of these cases are shown in Fig. 11.

In the case corresponding to Fig. 10(a) the contact trigonometric DSW is attached at its right edge to the cnoidal DSW. At the right soliton edge the cnoidal wave matches the right boundary plateau. The velocities of the characteristic points identified in Fig. 11(a) are given by

$$s_- = -\frac{1}{\delta} - \frac{1}{4\delta}\frac{[(\lambda_+^L)^2 - (\lambda_-^L)^2]^2}{(\lambda_-^L)^2 + (\lambda_+^L)^2},$$
$$s_+^{(1)} = -\frac{1}{\delta} + \frac{1}{4\delta}[3(\lambda_+^L)^2 + (\lambda_-^L)^2],$$
$$s_+^{(2)} = -\frac{1}{\delta} + \frac{1}{4\delta}[(\lambda_-^R)^2 + 2(\lambda_-^L)^2 + (\lambda_+^R)^2]. \tag{74}$$

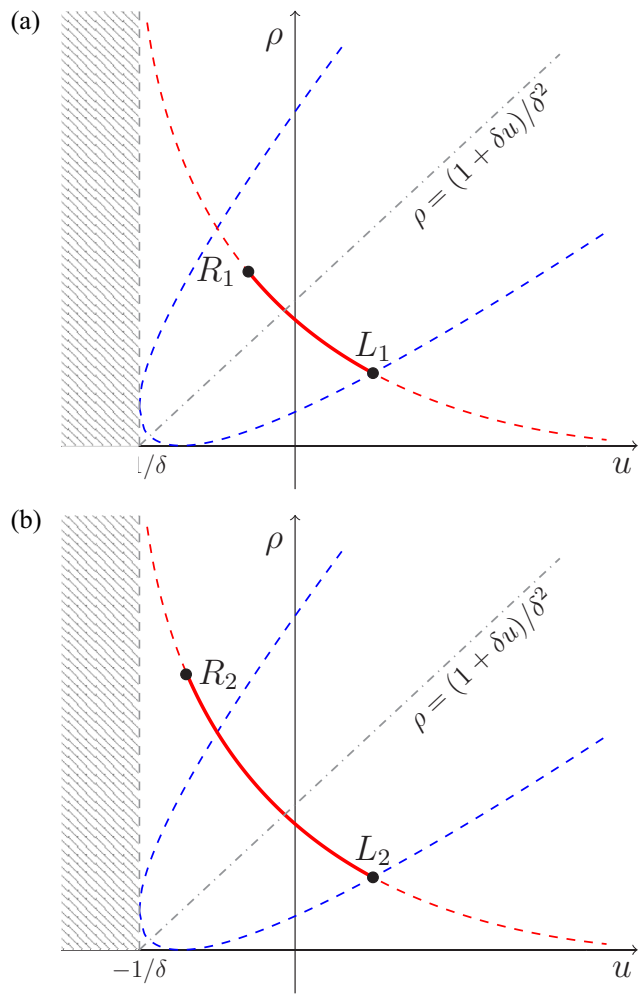

FIG. 10. Paths in the (u, I) plane associated with two types of combined shocks. The left and right boundary conditions correspond to points L and R, respectively; they lie on the curves along which the dispersionless Riemann invariant $r_+ = r_+^L = r_+^R$ ($\lambda_+ = \lambda_+^L = \lambda_+^R$) is constant. One has $r_-^L < r_-^R$ ($\lambda_-^L > \lambda_-^R$) in case (a) and $r_-^L > r_-^R$ ($\lambda_-^L < \lambda_-^R$) in case (b).

The resulting composite wave structure is shown in Fig. 12(a) (thin blue line) where it is compared with the numerical solution of the generalized CLL equation (2) (thick red line).

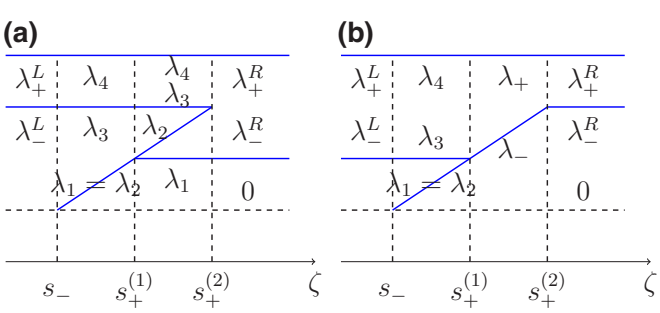

FIG. 11. Diagrams representing the evolution of the Riemann invariants as functions of $\zeta = x/t$ for combined shocks corresponding to the paths in the (u, ρ) plane shown in Fig. 10.

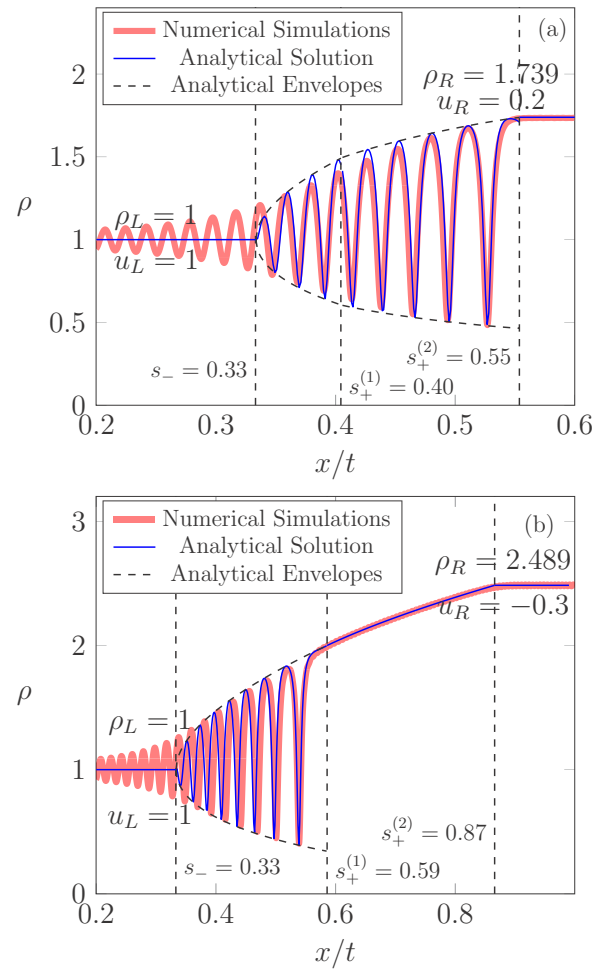

FIG. 12. The comparison of analytical (thin blue) and numerical (thick red) solutions of the generalized CLL equation (2) for combined shocks corresponding to the paths in the (u, ρ) plane (Fig. 10) and to the diagrams of Riemann invariants (Fig. 11). Here $\delta = 1$ and (a) $\rho^L = 1$, $u^L = 1$, $\rho^R = 1.739$, $u^R = 0.2$; (b) $\rho^L = 1$, $u^L = 1$, $\rho^R = 2.489$, $u^R = -0.3$. Dashed black lines show analytical envelopes. Vertical dashed lines indicate the edges of the combined DSW wave according to (74) and (75).

As an example, we take the boundary parameters $\rho^L = 1$, $u^L = 1$, $\rho^R = 1.739$, $u^R = 0.2$. For this parameter choice the solution consists of a combination of the cnoidal DSW (41) and part of the trigonometric DSW (44). The leading portion of the DSW consists of a modulated cnoidal wave. At the leading (soliton) edge, at $s_+^{(2)} = 0.55$, the modulus squared is $m = 1$, so solitons occur there. At the trailing edge of the cnoidal DSW, at $s_+^{(1)} = 0.40$, the modulus squared is $m = 0$, and trigonometric waves occur. The rear portion of the numerically realized shock consists of part of the contact DSW. It extends from its small-amplitude edge, at $s_- = 0.33$, where linear waves occur, to $s_+^{(1)} = 0.40$, where it matches the trailing edge of the cnoidal DSW. There is a discontinuity in the slope of the theoretical envelope at the junction of these two different DSW types for combined solutions. The vertical dashed lines in the figure separate the parts of the composite wave.

In the case corresponding to Fig. 10(b) the contact DSW is attached at its soliton edge to the rarefaction wave which matches at its right edge the right boundary plateau. The velocities of the characteristic points identified in Fig. 11(b) are expressed in terms of the boundary Riemann invariants by the formulas

$$s_- = -\frac{1}{\delta} - \frac{1}{4\delta}\frac{[(\lambda_+^L)^2 - (\lambda_-^L)^2]^2}{(\lambda_-^L)^2 + (\lambda_+^L)^2},$$
$$s_+^{(1)} = -\frac{1}{\delta} + \frac{1}{4\delta}[3(\lambda_-^R)^2 + (\lambda_+^L)^2],$$
$$s_+^{(2)} = -\frac{1}{\delta} + \frac{1}{4\delta}[3(\lambda_-^R)^2 + (\lambda_+^R)^2]. \quad (75)$$

The resulting combined wave structures are shown in Fig. 12(b) (thin blue lines) where they are compared with the numerical solution of the generalized CLL equation (thick red line). Here boundary parameters are $\rho^L = 1$, $u^L = 1$, $\rho^R = 2.489$, $u^R = -0.3$. For this parameter choice the approximate solution consists of the trigonometric DSW (44) and the rarefaction wave of (62) type. The leading edge of the DSW, at $s_+^{(1)} = 0.59$, consists of an algebraic soliton (45). At the left edge of the DSW, at $s_- = 0.33$, small-amplitude sinusoidal waves occur. The extent of rarefaction wave is $s_+^{(1)} < x/t < s_+^{(2)}$, where $s_+^{(1)} = 0.59$ and $s_+^{(2)} = 0.87$. One can see that agreement between numerical simulations and analytical results is very good.

This completes the characterization of all the key elements which may appear in a complex wave structure evolving from an arbitrary initial discontinuity of type (53). We can now proceed to the classification of all the possible composite structures.

V. CLASSIFICATION OF WAVE PATTERNS

Now we turn to the Riemann problem. This problem arose long ago and it remains an active area of research nowadays (see, e.g., [59–61]). As was noted above, one of the simplest cases is the KdV equation, where there are only two possible ways of evolution of initial discontinuity: it can evolve into either a rarefaction wave or cnoidal DSW. It was shown that the NLS equation evolution of any initial discontinuity leads to a wave pattern consisting of a sequence of building blocks two of which are represented by either the rarefaction wave or the DSW, and they are separated by a plateau, or a vacuum, or a two-phase self-similar solution close to an unmodulated nonlinear periodic wave. In total, there are six different possible wave patterns that can evolve from a given initial discontinuity. A similar classification of wave patterns was also established for the dispersive shallow water Kaup-Boussinesq equation [62,63]. For classification of wave patterns arising in solutions of the Riemann problem of the KdV or NLS type, it is important that the corresponding dispersionless limits are represented by the genuinely nonlinear hyperbolic equations. If this is not the case, then the classification of the KdV-NLS type becomes insufficient and it was found that it should include new elements—kinks, trigonometric dispersive shocks, or combined shocks. An example of such equations can be the modified KdV [56], Gardner [51], or Miyata-Camassa-Choi [64] equations. These new elements

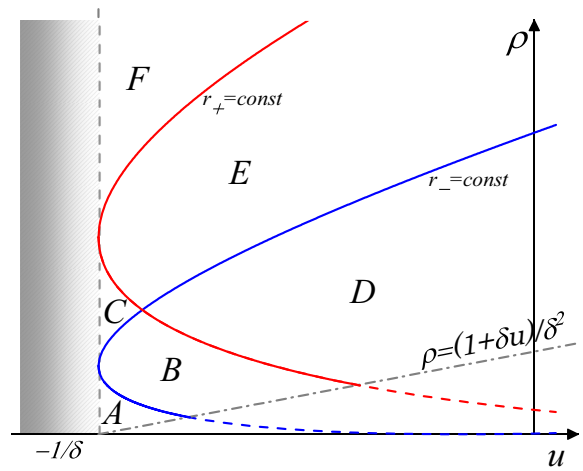

FIG. 13. Domains in the upper left monotonicity region of the (u, ρ) plane corresponding to different wave structures shown in Fig. 14.

can be labeled by two parameters only and therefore these possibilities can be charted on a two-dimensional diagram. In our present case the initial discontinuity (53) is parametrized by four parameters u^L, ρ^L, u^R, ρ^R; hence the number of possible wave patterns considerably increases and it is impossible to present them in a two-dimensional chart. Therefore it seems more effective to formulate the principles according to which one can predict the wave pattern evolved from a discontinuity with given parameters. A similar method was used [48,50] in the classification of wave patterns evolving from initial discontinuities according to the generalized NLS equation and the Landau-Lifshitz equation.

As is clear from the previous section, it is convenient to distinguish the situations where both points representing the left and right boundary conditions belong to the same region of monotonicity from those where they belong to different such regions (see Fig. 13). It is convenient to begin with the consideration of the classification problem from the case when both boundary points lie on one side of the line $\rho = (1 + \delta u)/\delta^2$ separating two monotonicity regions in the (u, ρ) plane. For definiteness, we denote the point of coordinates (u_L, ρ_L) referring to the left boundary by L and plot the two curves of constant Riemann invariants λ_+^L and λ_-^L. These divide the region into six subdomains. It is easy to see that when the point R referring to the right boundary is located in one of these domains (labeled by the symbols A, B, ..., F), one of the following inequalities is fulfilled:

$$\text{A: } \lambda_-^R < \lambda_+^R < \lambda_-^L < \lambda_+^L, \quad \text{B: } \lambda_-^R < \lambda_-^L < \lambda_+^R < \lambda_+^L,$$
$$\text{C: } \lambda_-^L < \lambda_-^R < \lambda_+^R < \lambda_+^L, \quad \text{D: } \lambda_-^R < \lambda_-^L < \lambda_+^L < \lambda_+^R,$$
$$\text{E: } \lambda_-^L < \lambda_-^R < \lambda_+^L < \lambda_+^R, \quad \text{F: } \lambda_-^L < \lambda_+^L < \lambda_-^R < \lambda_+^R. \quad (76)$$

The corresponding sketches of wave structures are shown in Fig. 14. In cases (B)–(E) two elementary wave structures presented in the previous section are connected by a plateau whose parameters are determined by the dispersionless Riemann invariants $\lambda_\pm^P$ equal to $\lambda_-^P = \lambda_-^R$ and $\lambda_+^P = \lambda_+^L$. In case (F) two rarefaction waves are separated by a region with

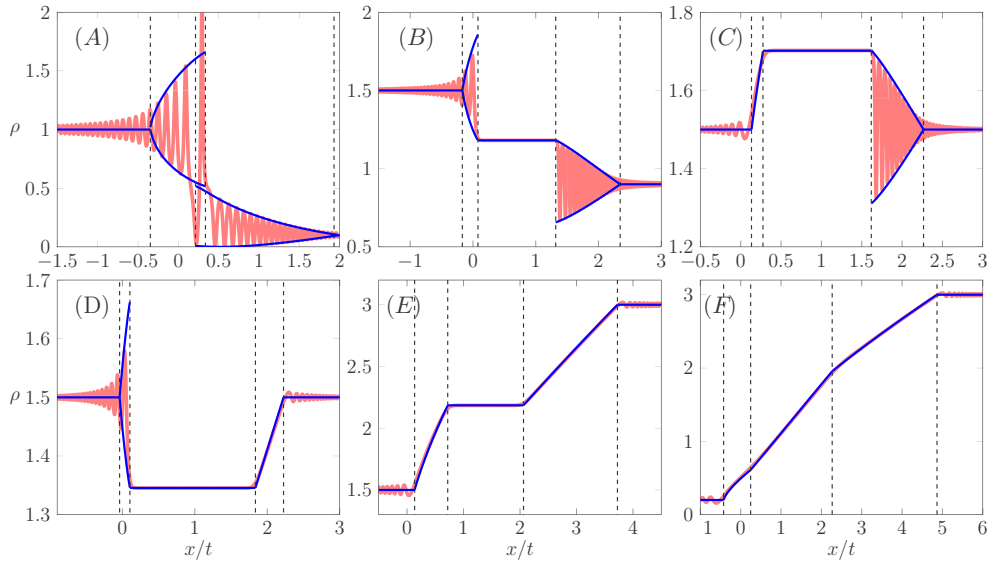

FIG. 14. Examples of wave structures corresponding to the location of the point R referring to the right boundary in one of the six domains shown in Fig. 13. In this case, the points corresponding to the boundaries of the initial state belong to one monotonicity region; therefore, the structures consist of a sequence of building blocks two of which are represented by either the rarefaction wave or the cnoidal DSW. Red (thick) curves show the numerical solution of the generalized CLL equation (2); blue (thin) curves illustrate the analytical solution. Vertical dashed lines reflect the edges of different waves.

intensity and chirp which are expressed by formulas

$$\rho = \frac{1+\delta\zeta}{\delta^2}, \quad u = -\frac{1}{\delta}. \tag{77}$$

The last property is a feature of the generalized CLL equation (2), since similar behavior for intensity (density for Bose-Einstein condensates or depth for water waves) was not previously observed.

Let us look at each case separately:

In case (A) two DSWs are produced with a nonlinear wave which can be presented as a nonmodulated cnoidal wave between them. The evolution of the wave structure is shown in Fig. 14(A).

In case (B) two DSWs are produced with a plateau between them. Here we have a collision of two light fluids [see Fig. 14(B)].

In case (C) we obtain a DSW on the right, a rarefaction wave on the left, and a plateau in between is produced [see Fig. 14(C)].

In case (D) we get the same situation as in case (C), but now the DSW and rarefaction wave exchange their places [see Fig. 14(D)].

In case (E) two rarefaction waves are connected by a plateau. Here rarefaction waves are able now to provide enough flux of the light fluid to create a plateau in the region between them [see Fig. 14(E)].

In case (F) two rarefaction waves are combined into a single wave structure where they are separated by a region with parameters varying according to (77). This means that two light fluids flow in opposite directions with velocities so large that the rarefaction waves are not able to form a plateau between them. A sketch of the wave structure is shown in Fig. 14(F).

Now we turn to consideration of the classification problem for the case when both boundary points lie below and to the right of the line $\rho = (1+\delta u)/\delta^2$. This situation is shown in Fig. 15. We see that the curves divide again this right monotonicity region into six domains. For this case the Riemann invariants can have the same orderings (76) as in the previous case. Depending on the location of the right boundary point in a certain domain, the corresponding wave structure will be formed. For all cases these structures coincide with those for the previous case. The only difference from the previous situation is structure (F), where in this case two rarefaction waves are combined into a single wave structure where they are separated by an empty region. This means that two light fluids flow in opposite directions with velocities so large that the rarefaction waves are not able to fill in an empty region between them.

At last, we have to investigate the situation when the boundary points are located on different sides of the line

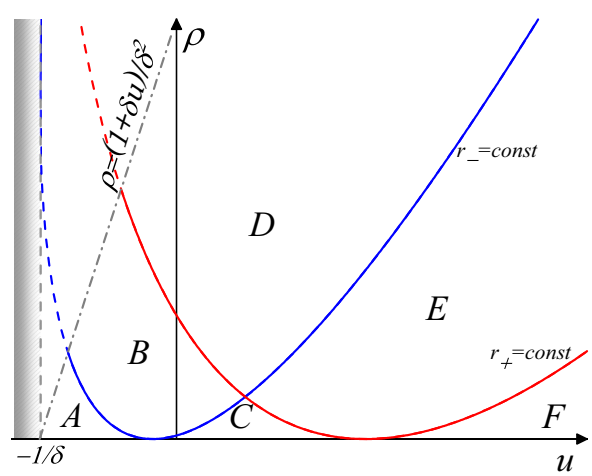

FIG. 15. Domains in the (u, ρ) plane on the lower right side of the line $\rho = (1+\delta u)/\delta^2$ corresponding to different structures.

$\rho = (1 + \delta u)/\delta^2$, that is, in different monotonicity regions. As we have seen in the previous section, in this case new complex structures consisting of contact DSWs or combined shocks appear. Since the total number of possible wave patterns is very large, we shall not list all of them here but rather illustrate the general principles of their classification.

For given boundary parameters, we can construct the curves corresponding to constant Riemann invariants $r_{\pm}^{L,R}$: each left or right pair of these parabolas crosses at the point L or R representing the left or right boundary state's plateau. Our task is to construct the path joining these two points; then this path will represent the arising wave structure. We already know the answer for the case when the left and right points lie on the same r curve. If this is not the case and the right point R lies, say, below the curve $r_{-}^{L} =$ constant then we can reach R by means of a more complicated path consisting of two curves joined at the point P. Evidently, this point P represents the plateau between two waves represented by the curves. At the same time, each curve corresponds to a wave structure discussed in the preceding section. In fact, there are two paths with a single intersection point that join the left and right boundary points. We choose the physically relevant path by imposing the condition that velocities of edges of all regions must increase from left to right. Having constructed a path from the left boundary point to the right one, it is easy to draw the corresponding λ diagram. To construct the wave structure, we use the formulas connecting the zeros ν_i of the resolvent with the Riemann invariants λ_i and expressions for the solutions parametrized by ν_i. This solves the problem of construction of the wave structure evolving from the initial discontinuity with given boundary conditions.

As an example of complex wave structure, we take the boundary conditions of the form $\rho_L = 1.2$, $u_L = -0.8$, $\rho_R = 0.6$, $u_R = 0$ with $\delta = 1$. It can be seen from the top panel of Fig. 16 that such initial conditions lie in different monotonicity regions. This means that one of the waves must consist of a contact DSW or of a combined shock wave. We have a plateau between the waves indicated by a single point P in Fig. 16. This plateau is characterized by two relations between Riemann invariants $r_{-}^{P} = r_{-}^{R}$ and $r_{+}^{P} = r_{+}^{L}$. Calculating the dispersionless Riemann invariants, we arrive at the diagram shown in the bottom panel of Fig. 16. It can be seen from this figure that the wave propagating to the left consists of a cnoidal wave ($s_1^L < \zeta < s_2^L$) and a contact wave ($s_2^L < \zeta < s_3^L$). In this case, the right wave consists of a rarefaction wave only ($s_1^R < \zeta < s_2^R$). Substitution of the dispersion Riemann invariants, which are the solution of the Whitham equations, into the periodic solution gives the wave structure, which is shown in Fig. 17. For comparison, a numerical solution is shown in red (thick curve). The vertical dashed lines correspond to the velocities s_1^L, s_2^L, s_3^L, s_1^R, and s_2^R. As we can see, analytical calculations agrees well with numerics.

We also give an example of a structure that illustrates the distinguishing feature of the generalized CLL equation (2). Let us take following boundary conditions: $\rho_L = 0.5$, $u_L = -1$, $\rho_R = 1.5$, and $u_R = -1$ with $\delta = 1$. In this case, the path in the (u, I) plane lies on the border with the region of modulation instability $u < -1/\delta$ (see the top panel in Fig. 18). Then the chirp u is constant and is equal to $u = -1/\delta = -1$. The Riemann invariants on the boundaries are equal: $r_{+}^{L} = r_{-}^{L}$

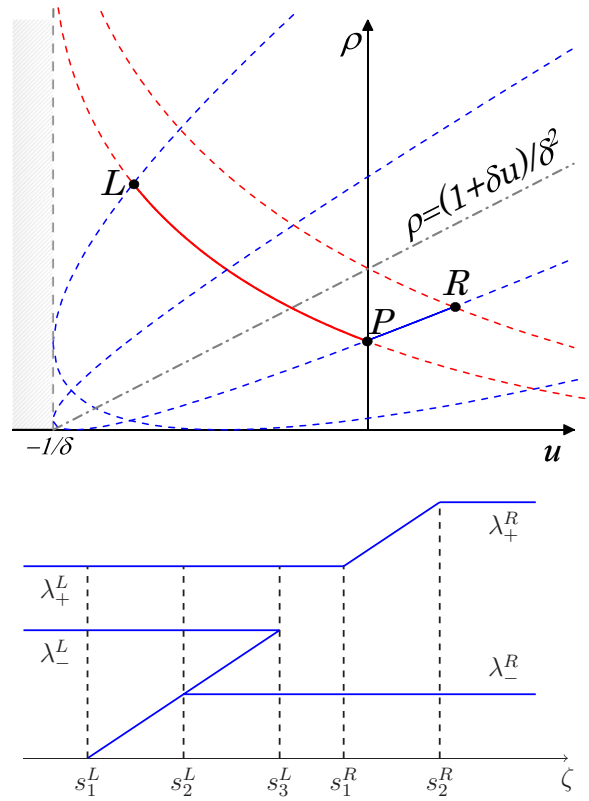

FIG. 16. Top panel: Relation between ρ and u for the simple wave solutions in the dispersionless regime for $\rho_L = 1.2$, $u_L = -0.8$, $\rho_R = 0.6$, and $u_R = 0$. Bottom panel: Diagram representing the evolution of the Riemann invariants as functions of $\zeta = x/t$ for complex structure.

and $r_{+}^{R} = r_{-}^{R}$. We can assume that for such initial conditions the Riemann invariants are equal everywhere. Then we get that the dependence of light intensity ρ on x is given by the first Eq. (77). A comparison of the numerical calculations with the analytical solution is shown in the bottom panel of Fig. 18.

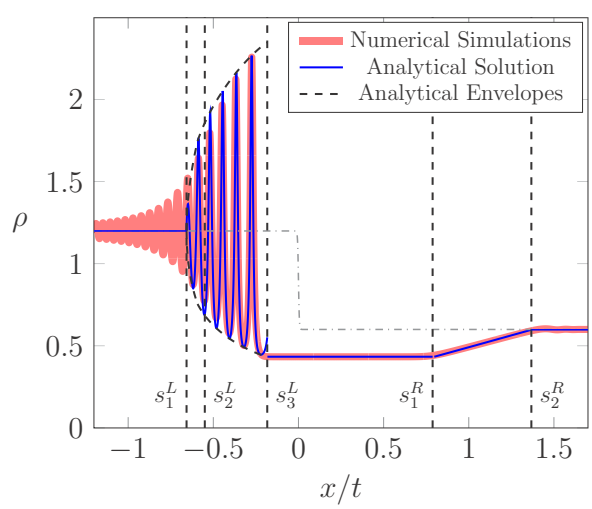

FIG. 17. Comparison of analytic (blue line) and numerical (red line) solutions for the initial profile (53) with $\rho_L = 1.2$, $u_L = -0.8$, $\rho_R = 0.6$, and $u_R = 0$.

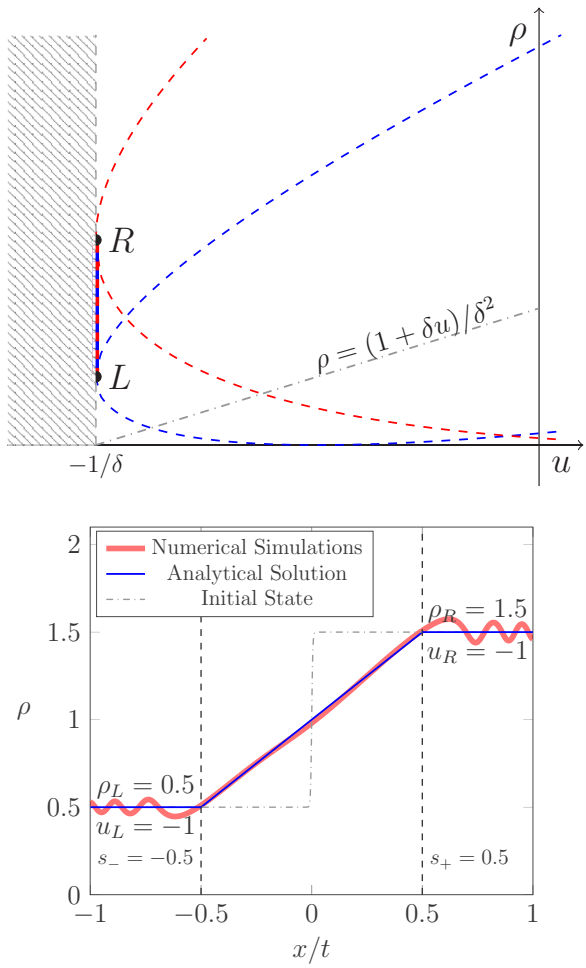

FIG. 18. Top panel: Path in the (u, I) plane for the initial profile (53) with $\rho_L < \rho_R$ and $u_L = u_R = -1/\delta$. The left and right boundary conditions correspond to points L and R, respectively. Bottom panel: Comparison of analytic (blue line) and numerical (red thick line) solutions for $\rho_L = 0.5$, $u_L = -1$, $\rho_R = 1.5$, and $u_R = -1$ with $\delta = 1$.

One can easily calculate the velocities of the wave edges

$$s_- = -\frac{1}{\delta} + \delta\rho_L, \quad s_+ = -\frac{1}{\delta} + \delta\rho_R. \tag{78}$$

The vertical dashed lines correspond to these velocities.

VI. CONCLUSION

In this work, the propagation of sufficiently long pulses in fibers is described by the generalized Chen-Lee-Liu equation, which is related to the class of the nonlinear Schrödinger equations modified by a self-steepening term. The Riemann problem of evolution of an initial discontinuity is solved for this specific case of nonconvex dispersive hydrodynamics. It is found that the set of possible wave structures is much richer than in the convex case and includes, as structural elements, trigonometric shock combined with rarefaction waves or cnoidal dispersive shocks. In the resulting scheme, one solution of the Whitham equations corresponds to two different wave patterns, and this correspondence is provided by a two-valued mapping of Riemann invariants to physical modulation parameters. To determine the pattern evolving from the given discontinuity, we have developed a graphical method.

In principle, one may hope that the results found here can be observed experimentally in systems similar to that used in the recent experiment [30]. However, one should keep in mind that in standard fibers in addition to the self-steepening effect, the Raman effect also occurs. However, the manifestations of these two effects are quite different and therefore they can be identified separately. As was shown in Ref. [65], the main consequence of the Raman scattering is the formation of stationary shock waves at finite length, while self-steepening leads to the formation of complex wave structures. At the same time, the generalized Chen-Lee-Liu theory is also used in the investigation of modulated wave dynamics of propagation through a single nonlinear transmission network, which presents some practical interest [47] (see also [66] where dispersive shock waves in transmission networks were studied). The method presented here is quite flexible and was also applied to other systems with nonconvex hydrodynamics [48–50].

ACKNOWLEDGMENTS

I would like to thank my teacher Anatoly Kamchatnov for introducing me to this topic and for useful discussions during the work on this paper. The reported study was funded by RFBR, Project No. 19-32-90011.

[1] A. M. Kamchatnov, *Nonlinear Periodic Waves and Their Modulations—An Introductory Course* (World Scientific, Singapore, 2000).
[2] G. A. El and M. A. Hoefer, Physica D (Amsterdam) **333**, 11 (2016).
[3] B. Riemann, Abh. Ges. Wiss. Göttingen, Math.-Phys. Kl. **8**, 43 (1860).
[4] W. J. M. Rankine, Philos. Trans. **160**, 277 (1870).
[5] H. Hugoniot, J. Ec. Polytech. **57**, 3 (1887).
[6] H. Hugoniot, J. Ec. Polytech. **58**, 1 (1889).
[7] N. E. Kotchine, Rend. Circ. Matem. Palermo **50**, 305 (1926).
[8] D. J. Korteweg and G. de Vries, Philos. Mag. **39**, 422 (1895).
[9] G. B. Whitham, Proc. R. Soc. London, Ser. A **283**, 238 (1965).
[10] A. V. Gurevich and L. P. Pitaevskii, Zh. Eksp. Teor. Fiz. **65**, 590 (1973) [Sov. Phys. JETP **38**, 291 (1974)].
[11] H. Flaschka, M. G. Forest, and D. W. McLaughlin, Commun. Pure Appl. Math. **33**, 739 (1980).
[12] C. S. Gardner, J. M. Green, M. D. Kruskal, and R. M. Miura, Phys. Rev. Lett. **19**, 1095 (1967).
[13] P. D. Lax, Commun. Pure Appl. Math. **28**, 141 (1974).
[14] S. P. Novikov, Funct. Anal. Appl. **8**, 236 (1974).
[15] I. M. Krichever, Funct. Anal. Appl. **22**, 200 (1988).
[16] S. P. Tsarev, Math. USSR Izvestia **37**, 397 (1991).
[17] B. A. Dubrovin and S. P. Novikov, Sov. Sci. Rev. C. Math. Phys. **9**, 58 (1993).

[18] W. J. Tomlinson, R. H. Stolen, and A. M. Johnson, Opt. Lett. **10**, 457 (1985).
[19] J. E. Rothenberg and D. Grischkowsky, Phys. Rev. Lett. **62**, 531 (1989).
[20] G. Xu, A. Mussot, A. Kudlinski, S. Trillo, F. Copie, and M. Conforti, Opt. Lett. **41**, 2656 (2016).
[21] G. Marcucci, D. Pierangeli, A. J. Agranat, R. Lee, E. DelRe, and C. Conti, *Nonlinear Optics (NLO), OSA Technical Digest* (Optical Society of America, 2019), paper NTu2A.3.
[22] J. Nuño, C. Finot, G. Xu, G. Millot, M. Erkintalo, and J. Fatome, Commun. Phys. **2**, 138 (2019).
[23] M. Isoard, A. M. Kamchatnov, and N. Pavloff, Phys. Rev. A **99**, 053819 (2019).
[24] G. Marcucci, D. Pierangeli, S. Gentilini, N. Ghofraniha, Z. Chen, and C. Conti, Adv. Phys.: X **4**, 1662733 (2019).
[25] M. G. Forest and J. E. Lee, in *Oscillation Theory: Computation and Methods of Compensated Compactness*, edited by C. Dafermos, J. L. Erickson, D. Kinderlehrer, and M. Slemrod, IMA Volumes on Mathematics and its Applications 2 (Springer, New York, 1986).
[26] M. V. Pavlov, Teor. Mat. Fiz. **71**, 351 (1987) [Theor. Math. Phys. **71**, 584 (1987)].
[27] V. E. Zakharov and A. B. Shabat, Zh. Eksp. Teor. Fiz. **61**, 118 (1971) [Sov. Phys. JETP **34**, 62 (1972)].
[28] A. V. Gurevich and A. L. Krylov, Zh. Eksp. Teor. Fiz. **92**, 1684 (1987) [Sov. Phys. JETP **65**, 944 (1987)].
[29] G. El, V. Geogjaev, A. Gurevich, and A. Krylov, Physica D (Amsterdam) **87**, 186 (1995).
[30] G. Xu, M. Conforti, A. Kudlinski, A. Mussot, and S. Trillo, Phys. Rev. Lett. **118**, 254101 (2017).
[31] W. Wan, S. Jia, and J. W. Fleischer, Nat. Phys. **3**, 46 (2007).
[32] G. A. El, A. Gammal, E. G. Khamis, R. A. Kraenkel, and A. M. Kamchatnov, Phys. Rev. A **76**, 053813 (2007).
[33] R. Hirota, J. Math. Phys. **14**, 805 (1973).
[34] A. Kundu, J. Math. Phys. **25**, 3433 (1984).
[35] F. Calogero and W. Eckhaus, Inverse Problems **3**, 229 (1987).
[36] K. Porsezian, M. Daniel, and M. Lakshmanan, J. Math. Phys. **33**, 1807 (1992).
[37] L. H. Wang, K. Porsezian, and J. S. He, Phys. Rev. E **87**, 053202 (2013).
[38] Y. S. Kivshar and G. P. Agrawal, *Optical Solitons: From Fibers to Photonic Crystals* (Academic Press, Amsterdam, 2003).
[39] S.-H. Han and Q.-H. Park, Phys. Rev. E **83**, 066601 (2011).
[40] D. J. Kaup and A. C. Newell, J. Math. Phys. **19**, 798 (1978).
[41] H. H. Chen, Y. C. Lee, and C. S. Liu, Phys. Scr. **20**, 490 (1979).
[42] V. S. Gerdjikov and M. I. Ivanov, Bulg. J. Phys. **10**, 130 (1983).
[43] C. Rogers and K. W. Chow, Phys. Rev. E **86**, 037601 (2012).
[44] J. Moses, B. A. Malomed, and F. W. Wise, Phys. Rev. A **76**, 021802(R) (2007).
[45] P. D. Lax, *Hyperbolic Partial Differential Equations* (AMS, 2006).
[46] M. G. Forest, C.-J. Rosenberg, and O. C. Wright, Nonlinearity **22**, 2287 (2009).
[47] W. H. Lin and E. Kenghe, *Schrödinger Equations in Nonlinear Systems* (Springer, Singapore, 2019).
[48] S. K. Ivanov and A. M. Kamchatnov, Phys. Rev. A **96**, 053844 (2017).
[49] A. M. Kamchatnov, J. Phys. Commun. **2**, 025027 (2018).
[50] S. K. Ivanov, A. M. Kamchatnov, T. Congy, and N. Pavloff, Phys. Rev. E **96**, 062202 (2017).
[51] A. M. Kamchatnov, Y.-H. Kuo, T.-C. Lin, T.-L. Horng, S.-C. Gou, R. Clift, G. A. El, and R. H. J. Grimshaw, Phys. Rev. E **86**, 036605 (2012).
[52] M. Wadati and K. Sogo, J. Phys. Soc. Jpn. **52**, 394 (1983).
[53] M. Abramowitz and I. A. Stegun, *Handbook of Mathematical Functions* (Dover Publications, New York, 1972).
[54] L. D. Landau and E. M. Lifshitz, *Fluid Mechanics* (Pergamon, Oxford, 1959).
[55] S. K. Ivanov and A. M. Kamchatnov, Zh. Eksp. Teor. Fiz. **151**, 644 (2017) [JETP **124**, 546 (2017)].
[56] T. R. Marchant, Wave Motion **45**, 540 (2008).
[57] Y. Kodama, V. U. Pierce, and F.-R. Tian, SIAM J. Math. Anal. **40**, 1750 (2008).
[58] G. A. El, M. A. Hoefer, and M. Shearer, SIAM Rev. **59**, 1 (2017).
[59] G. Biondini, Phys. Rev. E **98**, 052220 (2018).
[60] G. A. El, L. T. K. Nguyen, and N. F. Smyth, Nonlinearity **31**, 1392 (2018).
[61] L.-Q. Kong, L. Wang, D.-S. Wang, C.-Q. Dai, X.-Y. Wen, and L. Xu, Nonlinear Dyn. **98**, 691 (2019).
[62] G. A. El, R. H. J. Grimshaw, and M. V. Pavlov, Stud. Appl. Math. **106**, 157 (2001).
[63] T. Congy, S. K. Ivanov, A. M. Kamchatnov, and N. Pavloff, Chaos **27**, 083107 (2017).
[64] J. G. Esler and J. D. J. Pearce, Fluid Mech. **667**, 555 (2011).
[65] S. K. Ivanov and A. M. Kamchatnov, Opt. Spectrosc. **127**, 95 (2019).
[66] E. Kengne, A. Lakhssassi, T. Nguyen-Ba, and R. Vaillancourt, Can. J. Phys. **88**, 55 (2010).